

Bioinspired Hyperboloid Mechanical Metamaterial for Shock Absorption and Strain Regulation in Cartilage Remodeling

Jia Chen^{1#}, Qingqing Sun^{2#}, Yuliang Hou^{3#}, Shuaibing Liu¹, Litao Wang², Eshuang Deng¹, Liang Meng⁴, Xiaomeng Li^{2*}, Guoping Chen^{5*}, Jianglin Wang^{1*}

¹Department of Biomedical Engineering, Research Center for Intelligent Fiber Devices and Equipment, State Key Laboratory of New Textile Materials and Advanced Processing, Huazhong University of Science and Technology, Wuhan 430074, China.

²School of Mechanics and Safety Engineering, National Center for International Joint Research of Micro-nano Molding Technology, Zhengzhou University, Zhengzhou 450001, China.

³School of Mechanical and Power Engineering, Zhengzhou University, Zhengzhou 450001, Zhengzhou, China.

⁴State IJR Center of Aerospace Design and Additive Manufacturing, School of Mechanical Engineering, Northwestern Polytechnical University, Xi'an 710072, China.

⁵Research Center for Macromolecules and Biomaterials, National Institute for Materials Science, Ibaraki 305-0044, Japan.

[†]These authors contributed equally: Jia Chen, Qingqing Sun, Yuliang Hou

*Corresponding author. E-mail: jwang520@hust.edu.cn; Guoping.CHEN@nims.go.jp
xiaomeng.li@zzu.edu.cn

Abstract: Inspired by the shock-absorbing capabilities of natural insect elytra, we designed and fabricated a hyperboloid metamaterial exhibiting unique compression-torsion coupling behavior. This structure efficiently converts dynamic loads into strain energy, enabling high-strain elastic deformation. The hyperboloid lattice was integrated with a classic reticulation framework and filled with GelMA hydrogel, creating a tailored osteochondral scaffold with mechanical properties that closely match those of joint tissue. Under dynamic mechanical culture, compression-torsion stimulation in the hyperboloid zone induced high-strain elastic deformation, promoting chondrogenic differentiation of stem cells, while the more rigid reticulation zone, experiencing minimal deformation, facilitated osteogenic differentiation of stem cells. In a rabbit osteochondral defect model, hyperboloid-based shock-absorption scaffolds significantly enhanced the integrative repair of both cartilage and subchondral bone via the NF- κ B and calcium signaling pathways. The incorporation of the hyperboloid metamaterial, with its shock-absorbing and strain-regulating properties, demonstrates great potential for developing adaptable mechanical scaffolds for the cartilage

remodeling.

Keywords: Hyperboloid, Mechanical metamaterials, Shock absorption, Strain regulation, Mechanical stimulation, Cartilage remodeling.

1. Introduction

Nature is a master of materials, having created numerous metamaterials with exceptional microstructures and remarkable properties^[1]. The unique properties of metamaterials arise not from their base materials but from their intricately designed microstructures, which enable extraordinary physical properties such as negative refractive index, unusual wave velocity, and negative Poisson's ratio^[2, 3]. In biological tissue systems, structure and function are inseparably linked, a relationship honed over billions of years of evolution. Many biological tissues exhibit extraordinary properties that emerge from seeming ordinary biomaterials, owing to their hierarchical metastructure^[4].

Insect elytra, the lightweight yet hardened forewings of beetles, possess remarkable microstructural features that significantly contribute to their shock-absorbing capabilities. Upon impacted, the intricate geometry of the elytra deforms in a controlled manner, redistributing stress and preventing localized failure^[5]. This unique metastructure allows the elytra to protect the beetle's body from powerful external forces, providing a natural model for the development of advanced shock-absorbing metamaterials in engineering applications^[6]. In this study, we present the first discovery of the hierarchical arrayed ridge microstructure within the elytra and abstract a unique hyperboloid lattice microstructure. This structure consists of a three-dimensional arrangement of regularly spaced nodes interconnected by support rods, featuring highly repetitive and periodic geometric patterns capable of forming complex internal configurations.

Human joint tissue, a hierarchical structure composed of cartilage and subchondral bone, is frequently subjected to heavy stress and large strains. Despite advances in

regenerative medicine, healing joint injuries remains a significant challenge due to the complex stress-strain microenvironment^[7]. Increasing evidence suggests that tissue-engineered scaffolds hold considerable potential for repairing joint tissue lesions. However, due to the intricate mechanical environment of joint tissues, most current scaffolds fail to effectively adapt the high-strain and shock-loading conditions necessary for regenerative repair^[8]. In this study, elytra-inspired mechanical metamaterials offer a promising alternative for joint repair. These materials exhibit exceptional mechanical properties, including high specific strength, impact resistance, high energy absorption, and robust design flexibility.

The rapid advancement of bionics and 3D printing technologies has significantly accelerated the exploration and development of high-performance metamaterials^[9]. These innovations have paved the way for the continuous emergence of novel bionic designs that harness the unique capabilities of mechanical metamaterials. Recently, a new class of mechanically engineered metamaterials, characterized by exceptional tunability and distinctive properties, has emerged as a promising candidate in biomedical engineering^[10]. For example, metamaterial scaffolds designed with ultra-stiffness and a negative Poisson's ratio have been successfully applied in bone tissue engineering. Furthermore, these metamaterials can intelligently respond to external stimuli, enabling controlled drug release and offering significant potential in various biomedical applications^[11].

In this study, we drew inspiration from the structure of insect elytra to design and fabricate a hyperboloid metamaterial scaffold with exceptional shock-absorbing and strain-regulating properties. This scaffold is capable of mimicking the hierarchical mechanical properties of joint tissue. The mechanical stimuli generated by strain deformation promoted chondrogenic and osteogenic bi-differentiation of mesenchymal stem cells (MSCs). *In vivo* animal studies further demonstrated that the hyperboloid metamaterial scaffold, when combined with stem cells, effectively supports the synergistic repair of both cartilage and subchondral bone in joint tissue.

2. Results

2.1 Mechanical properties of hyperboloid lattice metamaterial

The elytra of flying insects not only provide protective function but also exhibit superior mechanical properties such as buffering, shock absorption and energy storage^[6, 12]. Inspired by the cross-sectional microstructure of elytra, a hyperboloid lattice metamaterial was abstracted and developed for potential applications in biomedical scaffolds (**Figure 1a, b**). The hyperboloid lattice designed in this study consist of three parallel and concentric hexagons maintaining consistent phase alignment. The hexagons are connected by diagonal rods that link the upper, middle, and lower sections. While the upper and lower hexagons are identical, the middle hexagon has a smaller side length, providing rotational freedom to the structure without interference during movement (**Figure 1c**).

Mechanical testing was used to evaluate hyperboloid lattices with different configurations. By varying the number of lateral supports ($s = 3, s = 6$), we investigated the mechanical strength of hyperboloid lattices with different shapes but the same rod diameter ($d = 0.4$ mm) (**Figure 1d**). The stress-strain curves of these two hyperboloid lattices were significantly different, and their compression modulus was 0.059 ± 0.003 MPa ($s = 3$) and 0.156 ± 0.027 MPa ($s = 6$), respectively (**Figure 1h, j**). In addition, the mechanical properties of the same shape hyperboloid lattices ($s = 6$) with different rod diameters were also investigated (**Figure 1e**). The mechanical strength of the lattices increased with increasing rod diameter, ranging from 0.040 ± 0.017 MPa ($d = 0.35$ mm) to 0.156 ± 0.027 MPa ($d = 0.4$ mm) and then to 0.246 ± 0.057 MPa ($d = 0.45$ mm) (**Figure 1i, k**). In the process of compression, the structural units of the hyperboloid lattice rotated and deformed, allowing for enhanced shock absorption (**Figure 1f**). Specifically, the hyperboloid lattice primarily exhibited three stages during compression: the linear elastic stage, the stress plateau stage, and the densification stage. In the linear elastic stage, the lateral supports rotated around the connecting points, and the interlayer framework simultaneously rotated. During this stage, the force increased linearly with displacement. In the stress plateau stage, the lateral supports began to bend

and deform, while the interlayer framework continued to rotate. The force remained nearly constant in this phase. In the densification stage, the lateral supports started to come into contact with each other, causing the force to rise sharply (**Video S7 and Video S8**). Finite element simulations further explained the displacement and stress distribution within the hyperboloid lattice under compressive load (**Figure 1g and Figure S2, Video S1 and Video S2**). Considering both mechanical strength and porosity, $s = 6$ and $d = 0.4$ mm were determined to be the optimal parameters for the hyperboloid lattice scaffolds.

Hyperboloid lattice metamaterial has the potential to be used as cartilage scaffold due to its unique shock absorption properties, while the reticulation lattice structure with high mechanical strength can provide the load-bearing function of subchondral bone (**Figure 2a**). The reticulation lattice consists of equidistant parallel rods stacked at varying angles (**Figure S3a**). Rod diameters (b) and stack angles (δ) affected the mechanical properties of the reticulation lattices (**Figure S3b, e**). The results showed that the mechanical strength of the lattices ($\delta = 90^\circ$) increased with the increase of the diameter of the rods (**Figure S3c, d**). For the same rod diameter ($b = 0.7$ mm), there was no significant difference in stress-strain curves and compression modulus (**Figure S3f, g**). Based on these results, we finally selected a printing rod diameter of 0.7 mm and angle of 90° were selected as the optimal parameters for the reticulation lattice scaffolds.

2.2 Construction and characterization of hyperboloid integrated scaffolds

The hyperboloid lattice was integrated with a classic reticulation lattice to create a hyperboloid integrated scaffold with mechanical mimicking and functional adaptation that closely match those of joint tissue. Using Boolean operation in SolidWorks, these two structures were merged to create a double-layered scaffold model with an overall height (H) of 5.8 mm and an outer diameter (D) of 7.3 mm (**Figure 2b**). In the printing process, different printing inks were applied to the upper and lower layers (**Figure S1**) to achieve distinct structural functions (**Figure 2c**). The hyperboloid integrated scaffold presented a clearly defined double-layer morphology, with a smooth surface on the upper hyperboloid structure and a rough, nHAP doping surface on the lower reticulation

structure (**Figure 2d and Figure S4**). Compared with the hyperboloid lattice, the compression strength of the hyperboloid integrated scaffold was improved (**Figure S5**). Furthermore, the stress-strain curves remained stable after 20 cycles of compression at 10% deformation, indicating the robust flexibility (**Figure 2g**). In addition, Finite element analysis further demonstrated that displacement and stress under compressive load were primarily concentrated in the upper hyperboloid structure, supporting its role in energy absorption and shock buffering (**Figure 2e, f and Video S3, Video S4**).

2.3 Hydrogel-filled hyperboloid osteochondral scaffolds

The hyperboloid osteochondral scaffold (HOS scaffold) was constructed by incorporating GelMA hydrogel into the hyperboloid integrated scaffold (**Figure 3a and Figure S6a, b**). The GelMA hydrogel demonstrated a uniform porous structure and maintained effective interfacial contact with the integrated scaffold (**Figure 3b**). Scanning electron microscopy revealed a clear distinction between the upper hyperboloid structure and the lower reticulation structure, with prominent nHAp particles visible on the reticulation surface (**Figure 3b**). Mechanical testing indicated that filling the scaffold with GelMA hydrogel significantly enhanced its compression modulus, from 0.231 ± 0.066 MPa to 0.81 ± 0.115 MPa (**Figure 3c, d**). During compression, the lateral supports of the integrated scaffold distorted and made the hexagon of the middle layer rotate. After the force unloading, the scaffold quickly rebounded to its original height without signs of damage or deformation (**Figure 3e**).

The HOS scaffold demonstrated high resilience under 10% strain loading, indicating that the hyperboloid structure endowed the hydrogel with the same damping and energy absorption functions (**Figure 3e**). Finite element simulation provided further insights into the scaffold's mechanical behavior. The hydrogel in the upper hyperboloid structure exhibited noticeable lateral expansion during compression (**Figure 3f-i and Figure S7**), while stress distribution remained concentrated in the upper layer, emphasizing the buffering capacity of the hyperboloid structure (**Figure 3f, h and Video S5, Video S6**). These results showed that the HOS scaffold with hyperboloid and reticulation structures has a gradient deformation effect. Experimental data closely matched simulation results, validating the accuracy of the simulation model (**Figure 3j, k**).

2.4 Hydrogel-filled hyperboloid osteochondral scaffolds for stem cell regulation

2.4.1 Dynamic compression evaluation

To investigate the influence of the HOS scaffold's mechanical properties on cellular behavior and fates, MSCs were encapsulated in the scaffolds and subjected to cyclic dynamic compression. The reticulation osteochondral scaffold (ROS scaffold) with both upper and lower layers of reticulation structure was prepared to exclude the effects of material composition (**Figure S8a-c**). Therefore, three scaffold types were prepared for comparison: HOS scaffolds loaded MSCs (with a hyperboloid upper layer and a reticulation lower layer), ROS scaffolds loaded MSCs (both the upper and lower layers are reticulation structure, but the upper layer did not contain nHAp) and GelMA hydrogel scaffolds loaded MSCs (with no internal 3D-printed structure) (**Figure S9**). These scaffolds were immersed in the culture medium and placed in a bioreactor that applied 5% strain at a frequency of 1Hz for 1 hour daily (**Figure S10**).

2.4.2 Mechanical stimulation on stem cell differentiation

Live/dead staining was performed on days 1, 4, and 7, and confocal fluorescence microscopy was used to assess cell viability. The results showed that MSCs maintained excellent activity across all scaffold types under static and dynamic culture conditions. However, cyclic dynamic compression promoted cell proliferation in all groups (**Figure S11a, b**). It has been reported that MSCs differentiate into chondrocytes at 5-10% strain stimulation and tend to differentiate into osteoblasts under minor strain microenvironment^[13]. Accordingly, it was hypothesized that MSCs in the hyperboloid upper layer would differentiate into chondrocytes, while those in the reticulation lower layer would differentiate osteoblasts (**Figure 4a**). This was verified by immunofluorescence staining, qPCR, Alcian blue, Safranin-O and Alizarin red staining conducted after 7 and 21 days of cell culture under cyclic dynamic compression. MSCs exhibited increased chondrogenic differentiation (SOX9, COL II) within the hyperboloid structure and osteogenic differentiation (Runx2, COL I) in the reticulation structure (**Figure 4b and Figure S12**). The qPCR results showed that under cyclic dynamic compression stimulation, both cartilage-related genes (SOX9, COL II) and osteogenesis-related genes (Runx2, COL I) were highly expressed in the HOS scaffolds (**Figure 4c-f**). Furthermore, Alcian blue, Safranin-O and Alizarin red staining confirmed that cyclic dynamic compression promoted the bidirectional differentiation of MSCs in the HOS scaffolds (**Figure S13**). The shock absorption properties of the

hyperboloid structure created a high-strain microenvironment conducive to chondrogenic differentiation, while the reticulation structure facilitated osteogenic differentiation.

2.4.3 Finite element analysis

Finite element analysis further confirmed that strain distribution within the scaffold (1/4 model of the scaffolds was used for analysis). PEGDA, PEGDA-nHA and GelMA hydrogel were assigned material properties using the parameters in [Table S1](#). The strain cloud maps of scaffolds were calculated by simulation and imported into MATLAB software to predict the areas of specific cell differentiation according to the model of the mechanical adjustment algorithm (**Figure 4g, h and Figure S14, Figure S15**). The mechanical adjustment algorithm found that mechanical cues can regulate the chondrogenic and osteogenic differentiation through formula **2.4.1**, specifically:

$$S = \frac{\gamma_{oct}}{a} + \frac{v}{b} \quad \mathbf{2.4.1}$$

Where a and b are constants, γ_{oct} is the octahedral shear strain, and v is the fluid velocity. Octahedral shear strain γ_{oct} can be calculated by formula **2.4.2**, namely:

$$\gamma_{oct} = \frac{1}{3} \sqrt{(\varepsilon_1 - \varepsilon_2)^2 + (\varepsilon_2 - \varepsilon_3)^2 + (\varepsilon_1 - \varepsilon_3)^2} \quad \mathbf{2.4.2}$$

Where ε_1 , ε_2 and ε_3 are the positive strains of the octahedron in the x, y and z directions, namely E_{11} , E_{22} and E_{33} , respectively. According to different values of S calculated by formula **2.4.1**, different units of scaffolds had different tissue differentiation results. S and its corresponding tissue differentiation results were shown in [Table S3](#).

According to the differentiation cloud maps, in the HOS scaffolds, cartilage differentiation was concentrated in hyperboloid structure layer, while differentiated mature bone was concentrated in the reticulation structure layer, exhibiting gradient osteochondral differentiation from top to bottom (**Figure 4g and Figure S14a**). Compared with the HOS scaffolds, the upper layer in the ROS scaffolds exhibited reduced cartilage differentiation but a higher presence of immature and mature bone. Additionally, fibrous connective tissue differentiation and bone absorption were more prevalent in the ROS scaffolds (**Figure 4h and Figure S14b**). When GelMA hydrogel alone was used as an osteochondral scaffold under dynamic loading, most MSCs in the

middle region of the scaffold differentiated into cartilage, while the upper and lower regions tended toward immature and mature bone (**Figure S15**). Notably, the capacity of GelMA Hydrogel alone to promote bone differentiation was significantly weaker than that of scaffolds incorporating lattice structures.

2.5 In vivo evaluation of hydrogel-filled hyperboloid osteochondral scaffolds

2.5.1 Macroscopic observation and micro-CT analysis

The rabbit osteochondral defect model was used to evaluate *in vivo* performance of the HOS scaffolds. The trochlear groove of the knee joint, a region subject to mechanical loading, was selected for scaffold implantation to allow for natural mechanical stimulation (**Figure 5a, b**). At 6 weeks post-implantation, macroscopic examination showed that the defect area in the HOS group was filled with newly formed tissue, integrating well with surrounding cartilage. In contrast, the ROS group showed partial filling of the defect, while both the GelMA and Blank groups exhibited visible defects without tissue integration (**Figure S16a**). By 12 weeks, the HOS group demonstrated substantial chondroid tissue formation with optimal repair outcomes among all groups. Although the ROS group achieved some integration with the surrounding cartilage, the GelMA group retained a large defect cavity, indicating the poorest repair effect (**Figure 5c**).

Micro-CT reconstruction illustrated an increase in new bone tissue over time in the defect area (**Figure 5d and Figure S16b**). The HOS and ROS groups exhibited significant subchondral bone repair, with a higher volume of new bone and distinct trabecular structures. In contrast, the GelMA group and Blank group exhibited limited self-repair capacity, with obvious cavities persisting in the defect sites (**Figure S16b**). Quantitative analysis revealed that bone volume fraction (BV/TV) and trabecular number (Tb.N) were significantly higher in the HOS group compared with other groups (**Figure S16c-e**). Although both the HOS and ROS groups had the same reticulation structure containing nHAp, the subchondral bone repair was superior in the HOS group. This suggests a synergistic effect between cartilage and bone repair in osteochondral regeneration (**Figure 5c, d and Figure S16a-e**).

2.5.2 Chondrogenesis and osteogenesis

Relative mRNA levels for chondrogenesis and osteogenesis genes in the HOS, ROS, GelMA, and Blank groups were evaluated via qRT-PCR (**Figure 5e and Figure S16f**). From 6 weeks to 12 weeks post-implantation, the expression levels of chondrogenesis genes and osteogenesis genes increased significantly, indicating continuous new cartilage and bone formation in the defect area. The chondrogenesis genes such as COL II and Aggrecan were upregulated in the HOS group, and their expressions were higher than those in the ROS group. Similarly, osteogenesis genes including COL I and OCN were also upregulated in the HOS group compared to the other groups. These findings suggested that the HOS scaffolds effectively promoted the synergistic regeneration of cartilage and bone *in vivo*.

2.5.3 Histological staining and immunofluorescence staining

Histological staining, including hematoxylin and eosin (H&E) (**Figure 5f and Figure S17a**) and Safranin O-fast green (S-F) (**Figure 5g and Figure S17b**) staining were performed to evaluate the quality of the newly formed osteochondral tissue at 6 weeks and 12 weeks post-surgery. At 6 weeks, the HOS group exhibited initial cartilage formation at the defect edges, while no cartilage tissue formation in other groups (**Figure S17b**). By 12 weeks, the HOS group demonstrated extensive new cartilage with intense Safranin O staining, indicating effective integration with adjacent cartilage (**Figure 5g**). Histological scoring based on the ICRS system confirmed superior osteochondral regeneration in the HOS group compared to other groups (**Figure S17c-f**). Immunofluorescence analysis of COL II further highlighted enhanced cartilage regeneration in the HOS group (**Figure 5h and Figure S18a**). In addition, immunofluorescence staining of COL I and Alizarin red staining showed new bone formation in the subchondral area in all groups except the Blank group (**Figure S18c, Figure S19**). Although the low degradation rate of PEGDA limited further cartilage generation, the HOS and ROS groups showed new cartilage and bone tissue, while fibrous tissue was produced in the defect area of the Blank group.

2.5.4 Proteomic analysis of new tissue in defect areas *in vivo*

Proteomic analysis was performed to investigate the molecular profile of newly formed tissue within the defect areas. Western Blot revealed that hyperboloid structure in the HOS scaffolds significantly enhanced the expression of chondrogenic protein (COL II, SOX9) and osteogenic proteins (COL I), compared with the ROS scaffolds. Meanwhile, the expressions levels of OCN, BMP2, RUNX2 and CD31 showed no significant differences between the two groups (**Figure S16g**). Further analysis of differentially expressed proteins (DEPs) was conducted through tandem mass tag (TMT) mass spectrometry, which highlighted an upregulation of cartilage-regenerative proteins, including COL4A1, COL10A1, TGF- β 3, and Piezo1, within the HOS group. Conversely, fibrosis-associated proteins, such as Lppr1, Fgf1, and Sparc, were notably downregulated (**Figure 5i**). KEGG pathway enrichment revealed that DEPs were enriched for functional annotations relating to NF- κ B, focal adhesion and calcium signaling pathways, as well as MAPK signaling pathway, IL-17 signaling pathway, ECM-receptor interaction (**Figure 5j**). The gene ontology (GO) analysis further implied a strong correlation of DEPs with collagen type IV trimer, collagen-containing ECM, and extracellular regions (**Figure S16h**). These results suggested that the deformation caused by the hyperboloid structure in the HOS scaffolds affects MSCs within the hydrogel, activating Piezo1 and altering their conformation to facilitate the influx of calcium ions. Elevated concentrations of calcium ions trigger intracellular calcium signaling pathways, resulting in increased secretion of TGF- β 3 and collagen, which promote the differentiation of MSCs into chondrocytes. Calcium signals also activate the NF- κ B signaling pathway, enhancing the anti-inflammatory properties of stem cells and promoting tissue regeneration (**Figure 5k**).

3. Discussion

The mechanical properties of natural articular cartilage and bone play a critical role in human movement^[14]. The upper cartilage layer possesses high elasticity and shock-absorbing capabilities, allowing it to effectively dissipate impact forces during movement and load-bearing activities^[15]. In contrast, the subchondral bone exhibits significant strength and rigidity, providing essential support under load-bearing

conditions^[16]. This integration of elasticity in the cartilage and rigidity in the underlying bone forms a mechanical synergy, allowing joints to adapt flexibly to various movements while maintaining structural stability under weight-bearing stress^[17].

Lattice metamaterials are a class of mechanical metamaterial characterized by a periodic arrangement of identical lattice structures in accordance with specific design rules^[18]. Inspired by the geometric configuration and mechanical behavior of biomaterials, there has been a surge in the design of high-performance lattice structures driven by biomimetic principles^[3, 19]. Inspiration from the microstructure of flying beetle elytra, a hyperboloid lattice metamaterial with unique chiral properties has been developed (**Figure 1**). The "compression-torsion" coupling effect of the hyperboloid lattice structure significantly enhances the load-bearing capabilities of the lattice scaffold. Its middle layer has a smaller design size, allowing for increased rotational freedom. Under axial compression, the lateral supports and the interlayer framework of the hyperboloid lattice rotate and deform, providing exceptional resistance to compression. Moreover, this structure demonstrates excellent vibration damping and energy absorption capabilities, similar to the function of cartilage tissue, highlighting its potential as a scaffold for cartilage regeneration^[20]. This innovative approach not only leverages biomimicry to enhance mechanical performance but also expands the possibilities for the development of advanced materials with diverse applications across engineering and biomedical fields. For instance, polyhedral scaffolds with varying structures offer adjustable mechanical strength and porosity, making them suitable for repairing a wide range of tissue types^[16].

In addition, GelMA hydrogel was incorporated into the lattice structure, which not only significantly improved the mechanical properties of the lattice structure, but also expanded its application in the biomedical field by providing biocompatible 3D microenvironment (**Figure 3**). Our results showed that hydrogel filling significantly reinforced the mechanical properties of hyperboloid and integrated scaffolds. This is because the filling of the hydrogel inhibits torsion of the lateral support and interlayer

framework of the hyperbolic structure, thus requiring greater force to achieve the same level of deformation as the unfilled scaffold. GelMA hydrogel, frequently used for *in vivo* tissue repair due to its excellent biocompatibility, typically has limited mechanical strength, which restricts its use in load-bearing applications^[21]. In this study, the combination of hydrogel makes hyperboloid integrated scaffold more suitable as an osteochondral scaffold for cartilage regeneration *in vivo*. MSCs encapsulated in hydrogel sense the same biochemical cues but different mechanical microenvironments, such as the graded distribution of strain, caused by the lattice structure under dynamic compressive load.

The osteochondral joint scaffold is subjected to dynamic compressive forces in the defect site due to the load of the knee joint movement. To investigate the biological response of hyperboloid osteochondral scaffolds carrying MSCs under dynamic loading, a bioreactor was employed to create a cyclic dynamic compression culture environment. The hyperboloid lattice structure, designed as a biomimetic cartilage layer, exhibits a unique "compression-torsion" property under compressive loads, which allows the filled hydrogel to experience a broad range of strain variations. This high-strain mechanical microenvironment encourages MSCs within the hydrogel to differentiate into chondrocytes^[22]. Additionally, the hyperboloid lattice structure efficiently absorbs most of the energy of dynamic loading for the underlying reticulation structure (biomimetic bone layer), thereby maintaining minor strain levels in the hydrogel surrounding the reticulation structure, which supports osteogenic differentiation (**Figure 4**). In contrast, typical reticulation structures (such as ROS scaffolds) lack the vibration absorption and energy absorption capabilities of hyperboloid lattice. Under compressive loads, reticulation structures often exhibit significant stress concentrations at the rod joints, leading to limited strain variation in the adjacent hydrogel. This fails to provide an optimal mechanical microenvironment for differentiating MSCs into chondrocytes but favors osteogenic differentiation^[23]. Overall, hyperboloid lattice structure offers a superior mechanical microenvironment in osteochondral tissue engineering scaffolds, promoting cartilage differentiation and greatly enhancing the

capability of osteochondral repair and regeneration.

In vivo animal models were utilized to further explore the induction and regeneration mechanisms of the HOS scaffolds carrying MSCs during osteochondral repair. The load of the knee joint varies with movement, with articular cartilage experiencing moderate pressure and tension during normal walking, at a deformation frequency of 1-5 Hz and a compression strain of 0.1-10%^[24]. Consequently, osteochondral scaffolds must adapt to the complex mechanical environment post-implantation *in vivo*. The upper layer of the HOS scaffolds with the similar Young's modulus to that of cartilage tissue (0.1~10 MPa), exhibits effective shock and energy absorption. These functions enable it to endure dynamic mechanical stimulation and convert it into strain variations, which activates multiple signaling pathways and promotes stem cell proliferation and cartilage differentiation.

Although both the ROS and the HOS scaffolds share the same biomimetic bone structure, their repair effects on subchondral bone are different, indicating that cartilage repair may affect the reconstruction of subchondral bone (**Figure 5**). These findings also clearly demonstrate a significant synergistic effect between cartilage and bone regeneration, highlighting the integration repair of osteochondral defects. Therefore, the HOS scaffold, combining a biomimetic cartilage layer (hyperboloid structure) with the bone layer (reticulation structure) from the perspective of mechanical regulation, supports cooperative cartilage and bone repair and holds strong potential for clinical application.

4. Conclusion

Inspired by the hierarchical structure of insect elytra, we designed and fabricated a hyperboloid mechanical metamaterial with outstanding mechanical properties, including shock absorption and energy storage. This rigid hyperboloid lattice was integrated with a soft hydrogel to create a hard-soft matrix with adjustable mechanical properties, optimized for joint tissue remodeling. The hyperboloid osteochondral joint scaffolds, characterized by compression-torsion coupling, generate a high-strain

mechanical microenvironment that modulates stem cell fates. *In vivo* evaluation using a rabbit osteochondral defect model further demonstrated that MSC-loaded HOS scaffolds significantly enhanced the integrative repair of both cartilage and subchondral bone via the NF- κ B and calcium signaling pathways. These findings highlight the remarkable potential of the hyperboloid metamaterial scaffold, with its shock-absorbing and strain-responsive properties, for use in tissue-engineering scaffolds with stress-stimulated regulation.

Acknowledgements

This work was financially supported by the, National Natural Science Foundation of China (32171323), National Key Research and Development Program of China (2022YFA1105100), the Fundamental Research Funds for the Central Universities (HUST: 2024JYCXJJ024), Interdisciplinary Research Program of HUST (2023JCYJ009), Shenzhen Science and Technology Program (JCYJ20241202125205007). Science, Technology, Innovation Commission of Shenzhen Municipality (KCXFZ20211020164544008).

Conflict of Interest: The authors declare No conflict of interest.

Data Availability Statement: All data needed to evaluate the conclusions in the paper are present in the paper and/or the Supplementary Materials. Additional data related to this paper may be requested from the authors.

Reference:

- [1] X.-S. Meng, L.-C. Zhou, L. Liu, Y.-B. Zhu, Y.-F. Meng, D.-C. Zheng, B. Yang, Q.-Z. Rao, L.-B. Mao, H.-A. Wu, S.-H. Yu, *Science* 2023, 380, 1252; M. Wu, Z. Shao, N. Zhao, R. Zhang, G. Yuan, L. Tian, Z. Zhang, W. Gao, H. Bai, *Science* 2023, 382, 1379.
- [2] Z. G. Nicolaou, A. E. Motter, *Nature Materials* 2012, 11, 608; X. Xin, C. Lin, B. Li, R. Zhang, C. Zeng, L. Liu, Y. Liu, J. Leng, *International Journal of Extreme Manufacturing* 2025, 7, 015506.
- [3] Y. Liu, Y. Wang, H. Ren, Z. Meng, X. Chen, Z. Li, L. Wang, W. Chen, Y. Wang, J. Du, *Nature Communications* 2024, 15, 2984.
- [4] M. Kalogeropoulou, A. Kracher, P. Fucile, S. M. Mihăilă, L. Moroni, *Advanced Materials* 2024, 36, 2408082; C. Wang, Z. Vangelatos, C. P. Grigoropoulos, Z. Ma, *Materials Today Advances* 2022,

13, 100206.

- [5] L. Meng, J. Shi, C. Yang, T. Gao, Y. Hou, L. Song, D. Gu, J. Zhu, P. Breitenkopf, W. Zhang, *Extreme Mechanics Letters* 2020, 40, 100869; W. Zhang, H. Yuan, N. Sun, H. Sun, X. Zhang, *Nature Communications* 2022, 13, 2937; S. Yu, X. Piao, N. Park, *Physical Review Letters* 2020, 125, 053901.
- [6] J. Rivera, M. S. Hosseini, D. Restrepo, S. Murata, D. Vasile, D. Y. Parkinson, H. S. Barnard, A. Arakaki, P. Zavattieri, D. Kisailus, *Nature* 2020, 586, 543.
- [7] L. Fu, L. Li, Q. Bian, B. Xue, J. Jin, J. Li, Y. Cao, Q. Jiang, H. Li, *Nature* 2023, 618, 740; Y. Liu, G. Dzidotor, T. T. Le, T. Vinikoor, K. Morgan, E. J. Curry, R. Das, A. McClinton, E. Eisenberg, L. N. Apuzzo, K. T. M. Tran, P. Prasad, T. J. Flanagan, S.-W. Lee, H.-M. Kan, M. T. Chorsi, K. W. H. Lo, C. T. Laurencin, T. D. Nguyen, *Science Translational Medicine*, 14, eabi7282.
- [8] Y. Yang, X. Zhao, S. Wang, Y. Zhang, A. Yang, Y. Cheng, X. Chen, *Nature Communications* 2023, 14, 7771; C.-Y. Lin, Y.-L. Wang, Y.-J. Chen, C.-T. Ho, Y.-H. Chi, L. Y. Chan, G.-W. Chen, H.-C. Hsu, D. W. Hwang, H.-C. Wu, S.-C. Hung, *Nature Biomedical Engineering* 2022, 6, 1105; L. Li, J. Yin, W. Ma, L. Tang, J. Zou, L. Yang, T. Du, Y. Zhao, L. Wang, Z. Yang, C. Fan, J. Chao, X. Chen, *Nature Materials* 2024, 23, 993.
- [9] W. Lin, M. Kluzek, N. Iuster, E. Shimon, N. Kampf, R. Goldberg, J. Klein, *Science* 2020, 370, 335; P. M. Lenggenhager, A. Stegmaier, L. K. Upreti, T. Hofmann, T. Helbig, A. Vollhardt, M. Greiter, C. H. Lee, S. Imhof, H. Brand, T. Kießling, I. Boettcher, T. Neupert, R. Thomale, T. Bzdušek, *Nature Communications* 2022, 13, 4373.
- [10] L. Du, W. Shi, H. Gao, H. Jia, Q. Zhang, M. Liu, Y. Xu, *Advanced Functional Materials* 2024, 34, 2314123; C. Coulais, D. Sounas, A. Alù, *Nature* 2017, 542, 461.
- [11] Q. Zhang, L. Ma, X. Ji, Y. He, Y. Cui, X. Liu, C. Xuan, Z. Wang, W. Yang, M. Chai, X. Shi, *Advanced Functional Materials* 2022, 32, 2204182.
- [12] T. Wei, M. Zhang, S. Lin, J. Ye, X. Yan, J. Guo, *Thin-Walled Structures* 2024, 196, 111543.
- [13] J. Yang, Y. S. Zhang, K. Yue, A. Khademhosseini, *Acta Biomaterialia* 2017, 57, 1.
- [14] B. Luo, S. Wang, X. Song, S. Chen, Q. Qi, W. Chen, X. Deng, Y. Ni, C. Chu, G. Zhou, X. Qin, D. Lei, Z. You, *Advanced Materials* 2024, 36, 2401009.
- [15] F. Yang, J. Zhao, W. J. Koshut, J. Watt, J. C. Riboh, K. Gall, B. J. Wiley, *Advanced Functional Materials* 2020, 30, 2003451.
- [16] H. Zhang, M. Zhang, D. Zhai, C. Qin, Y. Wang, J. Ma, H. Zhuang, Z. Shi, L. Wang, C. Wu, *Advanced Materials* 2023, 35, 2302716.
- [17] D. Liu, X. Wang, C. Gao, Z. Zhang, Q. Wang, Y. Pei, H. Wang, Y. Tang, K. Li, Y. Yu, Q. Cai, X. Zhang, *Advanced Materials* 2024, 36, 2409400.
- [18] H. Cui, D. Yao, R. Hensleigh, H. Lu, A. Calderon, Z. Xu, S. Davaria, Z. Wang, P. Mercier, P. Tarazaga, X. Zheng, *Science* 2022, 376, 1287; X. Zheng, H. Lee, T. H. Weisgraber, M. Shusteff, J. DeOtte, E. B. Duoss, J. D. Kuntz, M. M. Biener, Q. Ge, J. A. Jackson, S. O. Kucheyev, N. X. Fang, C. M. Spadaccini, *Science* 2014, 344, 1373.
- [19] Y. Wang, K. Wu, X. Zhang, X. Li, Y. Wang, H. Gao, *Science Advances*, 10, eadq2664; A. Djellouli, B. Van Raemdonck, Y. Wang, Y. Yang, A. Caillaud, D. Weitz, S. Rubinstein, B. Gorissen, K. Bertoldi, *Nature* 2024, 628, 545; C. E. Gregg, D. Catanoso, O. I. B. Formoso, I. Kostitsyna, M. E. Ochalek, T. J. Olatunde, I. W. Park, F. M. Sebastianelli, E. M. Taylor, G. T. Trinh, K. C. Cheung, *Science robotics*, 9, eadi2746.
- [20] R. C. Nordberg, B. J. Bielajew, T. Takahashi, S. Dai, J. C. Hu, K. A. Athanasiou, *Nature Reviews*

Rheumatology 2024, 20, 323; H. Zhou, Z. Zhang, Y. Mu, H. Yao, Y. Zhang, D.-A. Wang, ACS Nano 2024, 18, 10667.

[21] P. Xiang, M. Jiang, X. Chen, L. Chen, Y. Cheng, X. Luo, H. Zhou, Y. Zheng, Advanced Science 2024, 11, 2305856.

[22] N. D. Caprio, M. D. Davidson, A. C. Daly, J. A. Burdick, Advanced Materials 2024, 36, 2312226.

[23] J. Na, C. Tai, Z. Wang, Z. Yang, X. Chen, J. Zhang, L. Zheng, Y. Fan, Biomaterials 2025, 312, 122715.

[24] Y. Hua, H. Xia, L. Jia, J. Zhao, D. Zhao, X. Yan, Y. Zhang, S. Tang, G. Zhou, L. Zhu, Q. Lin, Science Advances, 7, eabg0628; J. Lee, O. Jeon, M. Kong, A. A. Abdeen, J.-Y. Shin, H. N. Lee, Y. B. Lee, W. Sun, P. Bandaru, D. S. Alt, K. Lee, H.-J. Kim, S. J. Lee, S. Chaterji, S. R. Shin, E. Alsberg, A. Khademhosseini, Science Advances, 6, eaaz5913.

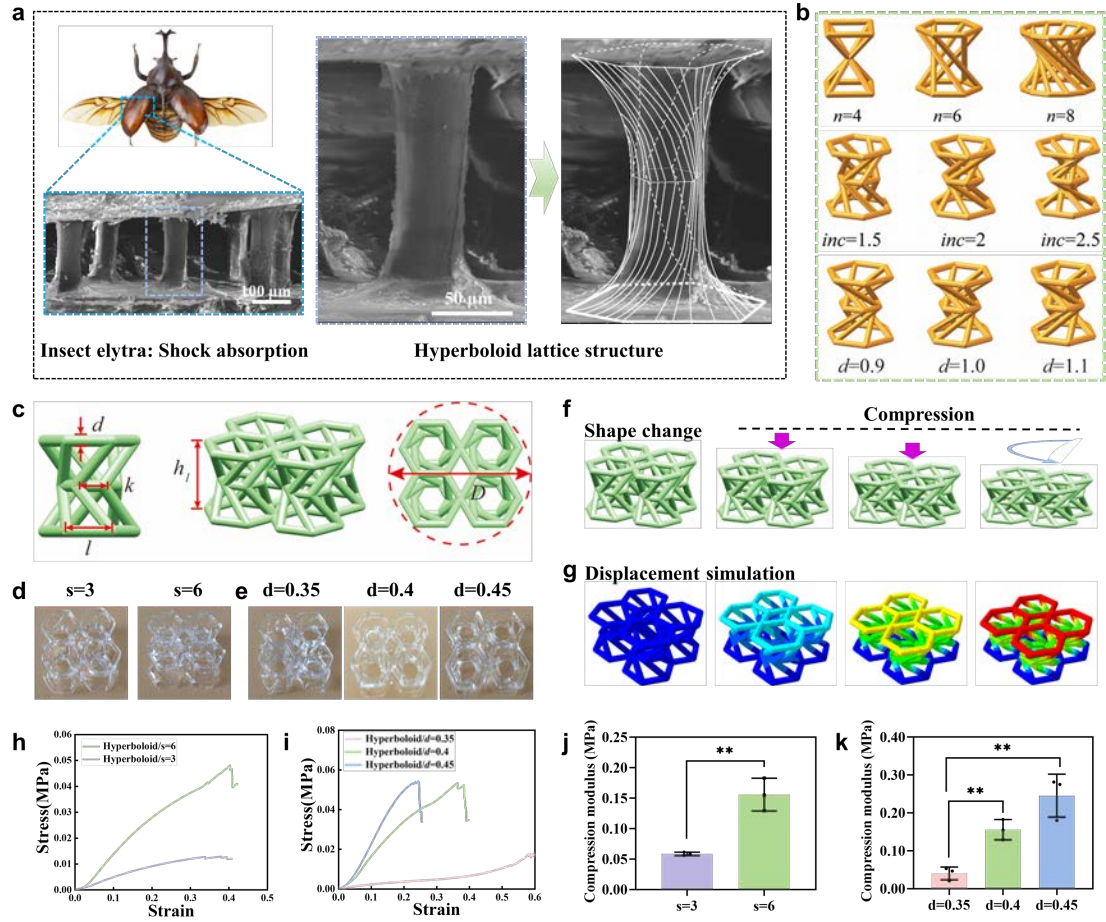


Figure 1. Design and mechanical evaluation of hyperboloid lattice structure. (a) Hyperboloid lattice structure inspired by insect elytra has the advantages of buffering, energy storage and shock absorption. (b) Various types of hyperboloid lattice structures inspired by the elytra structure. (c) The design model and parameters of hyperboloid lattice structures. (d) Hyperboloid lattice structures with different number of skew rods ($s = 3$ and $s = 6$) were prepared by 3D printing technology. (e) Hyperboloid lattice structures with different rod diameter ($d = 0.35$ mm, $d = 0.4$ mm and $d = 0.45$ mm) were prepared by 3D printing technology. (f) In the process of compression, the skew rods of the hyperboloid lattice structure enabled to rotate and deform to provide shock absorption. (g) The commercial finite element software ABAQUS was used to simulate the deformation of the hyperboloid lattice structure under compressive load. (h, j) The compression modulus of hyperboloid lattice structures with different skew rods were 0.059 ± 0.003 MPa ($s = 3$) and 0.156 ± 0.027 MPa ($s = 6$), respectively. (i, k) The compression modulus of hyperboloid lattice structures with different rod diameter were 0.040 ± 0.017 MPa ($d = 0.35$ mm), 0.156 ± 0.027 MPa ($d = 0.4$ mm) and 0.246 ± 0.057 MPa ($d = 0.45$ mm), respectively.

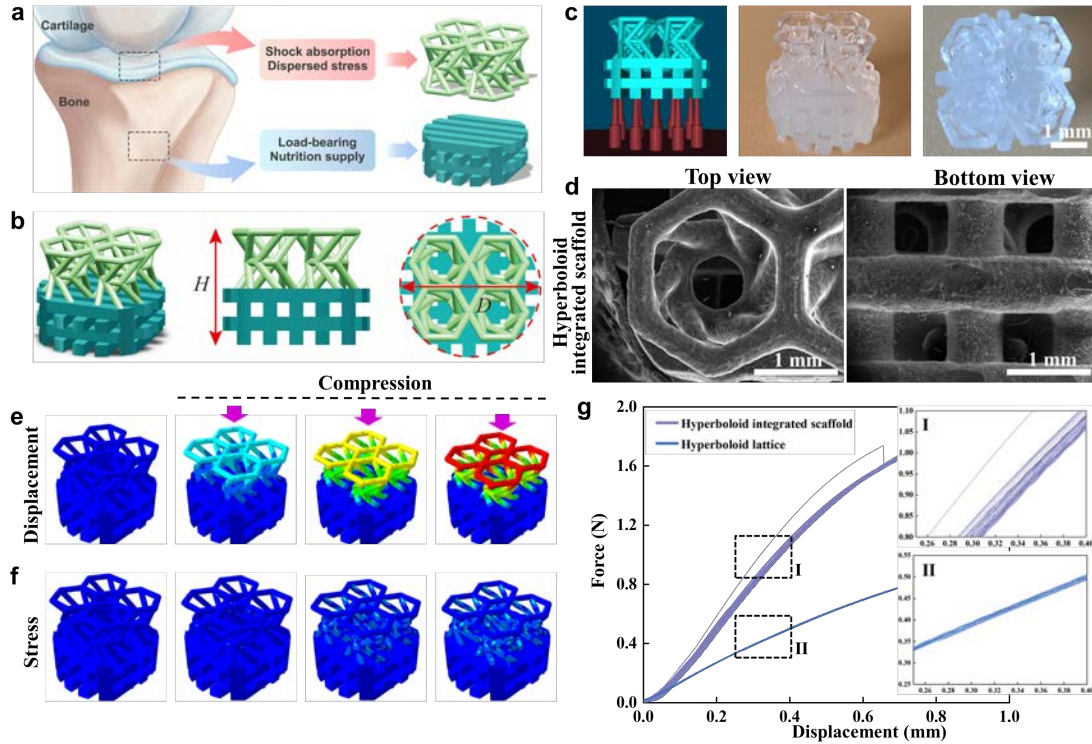


Figure 2. Design and mechanical evaluation of hyperboloid integrated scaffolds. (a) Hyperboloid structure has the potential to be used as cartilage scaffold due to its unique shock absorption properties, while the load-bearing properties of subchondral bone require high strength reticulation structure to be adapted. (b) Combining the hyperboloid structure with the reticulation structure exhibited a gradient and integrated scaffold for osteochondral repair. (c) Hyperboloid integrated scaffold with optimal parameters was printed by 3D printing technology. (d) SEM images of the top and bottom views for the hyperboloid integrated scaffold. (e, f) The finite element analysis was used to simulate the deformation and stress of the hyperboloid integrated scaffold under compressive load. The deformation of the hyperboloid integrated scaffold under compressive load was primarily concentrated in the hyperboloid structure of the upper layer. (g) The displacement and force changes in the hyperboloid lattice structure and hyperboloid integrated scaffold were separately assessed during cyclic compression.

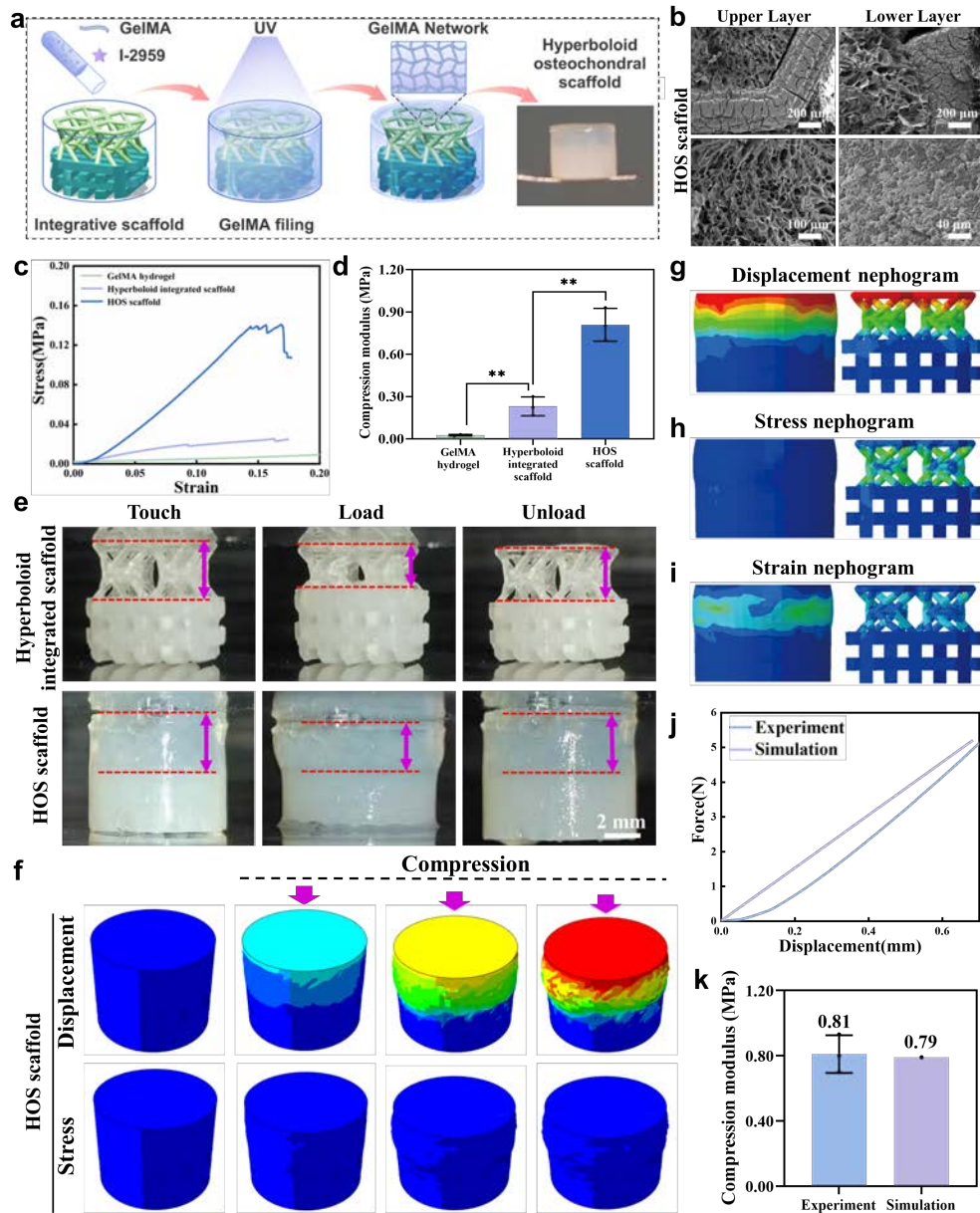


Figure 3. Hyperboloid integrated scaffolds filled with GelMA hydrogel. (a) Schematic diagram showed the hyperboloid integrated scaffold immersed in the GelMA precursor solution was activated to form hyperboloid osteochondral scaffold. (b) SEM images confirmed the GelMA hydrogel were uniform distributed in the upper and lower layers of the hyperboloid integrated scaffold. (c, d) Stress-strain curves demonstrated the scaffold-enhanced hydrogel significantly enhanced its compression modulus. (e) The HOS scaffold could recover to the initial height after 10% strain loading, and no damage deformation such as fracture was found. (f) Finite element analysis (FEA) revealed the injected hydrogel expanded laterally and produce large deformation in the upper hyperboloid layer, but no significant change in the lower reticulation layer. (g-i) The displacement, stress and strain nephograms of FEA showed that most of stress were laden in the lateral supports and the force of hydrogel did not change. (j) The force-displacement curve obtained by FEA was in good agreement with the experimental data. (k) The difference between the compression modulus measured by experiments and that calculated by simulation was only 0.02MPa.

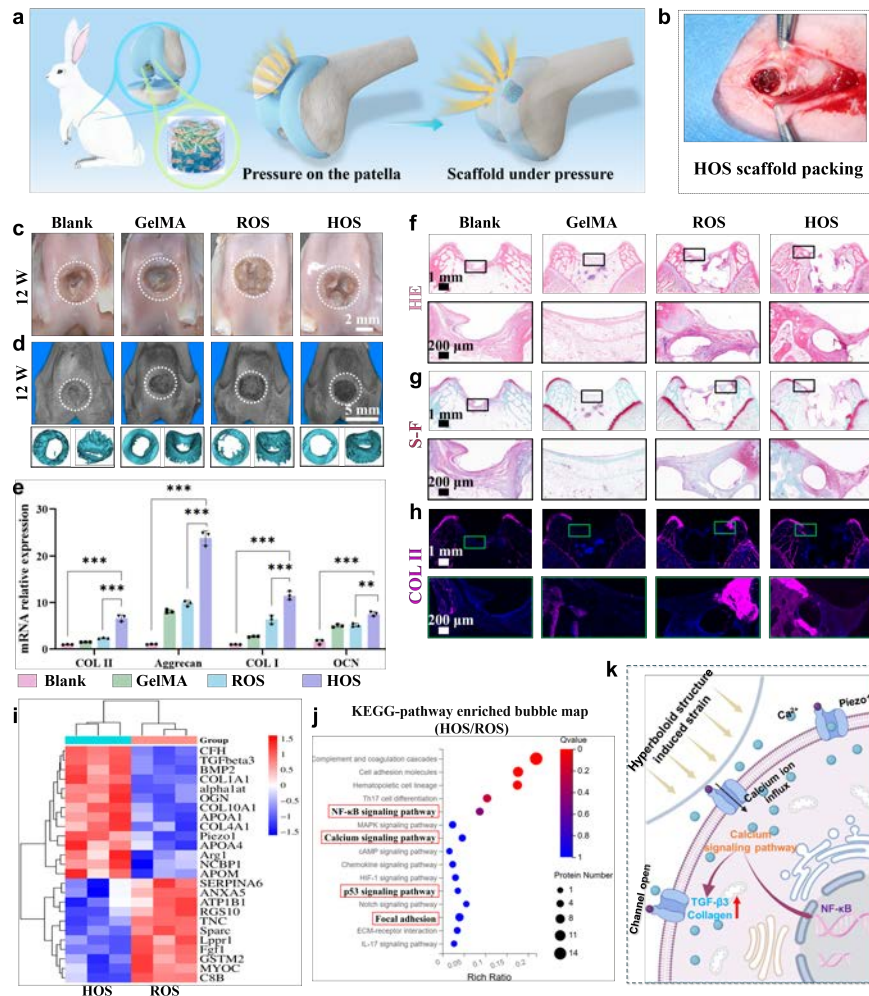


Figure 5. Hyperboloid osteochondral scaffolds loaded with MSCs promoted osteochondral remodeling in rabbits. (a) The HOS scaffold implanted in the rabbit knee defect was frequently stimulated by the stress during the native motion. (b) A cylindrical defect with 5 mm in diameter and 4 mm in depth was created for scaffold implantation at the trochlear groove of the knee joint. (c) Macroscopic appearance showed that the cartilage repair in the HOS group was superior to that in other groups after 12 weeks post-surgery. (d) Micro-CT evaluation demonstrated the subchondral bone in the HOS group was optimal. (e) The qRT-PCR results showed that the expression levels of cartilage-associated genes (COL II and aggrecan) and osteogenesis-associated genes (COL I and OCN) were the highest in the HOS group. (f-h) Hematoxylin and eosin (H&E), Safranin-O/fast green (S-F) and immunohistochemical staining of collagen II revealed the consistent results. (i) Heatmap represented the osteochondral associated proteins were increased in the HOS group, including TGFβ3, BMP2, Piezo1, COL4A1 and COL10A1, while the fibrosis-associated proteins were decreased, including Lppr1, Fgf1 and Sparc. (j) KEGG enrichment analysis verified the regulation pathway of HOS scaffold was associated with NF-κB signaling pathway and calcium signaling pathway. (k) The deformation induced by the hyperboloid structure modulated MSCs by activating Piezo1 and altering their conformation to facilitate the influx of calcium ions. Elevated calcium ion concentrations trigger intracellular calcium signaling pathways, leading to increased secretion of collagen and TGF-β3, while also activating NF-κB signaling pathways to enhance anti-inflammation.

Supporting Information

Bioinspired Hyperboloid Mechanical Metamaterial for Shock Absorption and Strain Regulation in Cartilage Remodeling

Jia Chen^{1#}, Qingqing Sun^{2#}, Yuliang Hou^{3#}, Shuaibing Liu¹, Litao Wang², Eshuang Deng¹, Liang Meng⁴, Xiaomeng Li^{2*}, Guoping Chen^{5*}, Jianglin Wang^{1*}

¹Department of Biomedical Engineering, Research Center for Intelligent Fiber Devices and Equipment, State Key Laboratory of New Textile Materials and Advanced Processing, Huazhong University of Science and Technology, Wuhan 430074, China.

²School of Mechanics and Safety Engineering, National Center for International Joint Research of Micro-nano Molding Technology, Zhengzhou University, Zhengzhou 450001, China.

³School of Mechanical and Power Engineering, Zhengzhou University, Zhengzhou 450001, Zhengzhou, China.

⁴State IJR Center of Aerospace Design and Additive Manufacturing, School of Mechanical Engineering, Northwestern Polytechnical University, Xi'an 710072, China.

⁵Research Center for Macromolecules and Biomaterials, National Institute for Materials Science, Ibaraki 305-0044, Japan.

I. Experimental section

1. Materials

Polyethylene glycol diacrylate (PEGDA, Mw = 600), gelatin, nano-hydroxyapatite (nHAp, size = 100 nm) and 2-hydroxy-4'-(2-hydroxyethoxy)-2-methylphenylacetone (I2959) were purchased from Aladdin Biochemical Co., Ltd. (Shanghai, China). Methacrylic anhydride (MA, 94% purity) was obtained from Macklin Biochemical Co., Ltd. (Shanghai, China). 2,4,6-trimethylbenzoyl diphenyl phosphine oxide (TPO, purity: $\geq 99\%$) was sourced from Shanghai Yinchang New Materials Co., Ltd. The mesenchymal stem cells (MSCs) were kindly provided by the Affiliated Hospital of Zhengzhou University (Zhengzhou, China). bFGF protein was purchased from Thermo

Fisher Co., Ltd. DMEM/F12 cell culture medium, cartilage differentiation medium and osteogenic differentiation medium from Pricella Life Technology Co., Ltd. (Wuhan, China). SOX9 and Runx2 antibodies were purchased from Abcam, and COL II and COL I antibodies were sourced from Arigo Biolaboratories Corp. All other chemical and biological reagents were used as received.

2. Model design of hyperboloid lattice structure

The hyperboloid lattice structure was designed using SolidWorks software (Dassault Corporation, USA). The parameters of the hyperboloid lattice were as follows: the side length of upper and lower hexagon (l) was 1.5 mm, with the middle hexagon length (k) of 0.9 mm. The torsion degree of the lateral support (inc) was set at 2, the height of the structure (hl) is 3 mm. The number of lateral supports (s) and the rod diameter (d) of the hyperboloid structure were adjustable. The scaffold with desired size could be achieved by periodically repeating the unit cells.

The reticulation lattice structure consists of equidistant, parallel rods stacked vertically, where the width of the rods (b) and the acute angle (δ) between adjacent layers of rods are adjustable. The overall outline structure of the structure was cylindrical, with a diameter (D) of 7.3 mm and a height ($h2$) of 2.8 mm. By using Boolean operations in SolidWorks, the hyperboloid and reticulation structures were combined to form the final hyperboloid integrated scaffold model. The lower side supports of the hyperboloid structure were inserted into the bottom layer, allowing for the hyperboloid structure's energy absorption to complement the reticulation structure's load-bearing capabilities.

3. Fabrication of hyperboloid osteochondral scaffold

The 3D printing of the scaffolds was conducted using a commercial Digital Light Processing (DLP) 3D printer and its accompanying slicing software (Photo Workshop). The bioink used for the hyperboloid structure was PEGDA with 1% (w/w) TPO, while the reticulation structure was printed using PEGDA with 1% (w/w) TPO and 2% (w/w) nHAp. The printing parameters were set as follows: the layer thickness was 50 μ m with

an exposure time of 3 seconds per layer. The hyperboloid and reticulation structures were printed separately under the above conditions. For the hyperboloid integrated scaffold, which consists of different materials for the upper and lower layers, printing was paused after the completion of the lower layer to allow for the ink change before continuing with the upper hyperboloid layer. After completing the printing process, the scaffold was carefully removed from the printing plate. Then, any residual printing solution was washed off using alcohol, resulting in clean and intact scaffolds for further use.

To further optimize the mechanical properties of the scaffolds and provide a 3D microenvironment for cells, GelMA hydrogel was selected to fill the 3D-printed lattice. GelMA macromonomers were synthesized using gelatin and methacrylic anhydride (MA). The chemical structures of both GelMA and gelatin were confirmed using nuclear magnetic resonance (NMR) spectroscopy, with ¹HNMR spectra acquired at 300MHz (Tokyo JEOL Co., LTD., Japan). The hyperboloid integrated scaffold was sterilized and then placed into a custom silicone mold matching the scaffold's height and outer diameter. GelMA hydrogel precursor solution (10 wt%) was slowly added into the mold until the scaffold was completely immersed. The hydrogel precursor solution was then crosslinked by exposure to 365 nm ultraviolet (UV) light for 2 minutes to prepare a hyperboloid osteochondral scaffold (HOS scaffold).

4. Physicochemical characterization of hyperboloid osteochondral scaffold

Photographs were taken to capture the general morphology of all scaffolds while scanning electron microscopy (SEM) was used for detailed microstructural analysis. The scaffolds were first immersed in phosphate-buffered saline (PBS) solution and incubated at 37°C until reaching swelling equilibrium. After rinsing with deionized water, the scaffolds were placed in a refrigerator at -80°C overnight and subsequently freeze-dried. SEM imaging was performed on the top, bottom, and cross-sectional surfaces of each scaffold group to analyze the microstructural characteristics.

The hyperboloid lattice structures with varying design parameters were fabricated to investigate their mechanical properties. For comparison, the reticulation lattice and their hydrogel composite scaffolds with identical dimensions ($D = 7.3\text{mm}$, $h = 3\text{ mm}$) and materials (PEGDA with 1% TPO) were also prepared, designated as Reticulation/Up scaffold and Reticulation/Up-Hydrogel scaffold, respectively. All mechanical tests were conducted using an electronic universal material testing machine (CTM). Prior to testing, the scaffolds were immersed in PBS to reach swelling equilibrium. The prepared scaffolds were positioned on the universal testing machine and compressed at a speed of 0.5 mm/min until failure, producing a stress-strain curve for each scaffold. The Young's modulus of the scaffolds was calculated as the slope of the linear elastic region of the stress-strain curve ($n = 3$). In the cyclic compression experiments, the scaffolds were initially compressed at a speed of 0.5 mm/min , then unloaded to the starting position at a speed of 2 mm/min . This loading-unloading cycle was repeated 20 times to generate the cyclic compression curve of the scaffolds, allowing assessment of their resilience and flexibility under repeated load.

5. Finite element simulation of hyperboloid osteochondral scaffold

Finite element analysis (FEA) was conducted to assess the mechanical properties of hyperboloid osteochondral scaffold under compressive load, using the commercial software ABAQUS. The simulated stress-strain curves were compared to experimental data for validation. Given the small displacement, the Hooke model was applied to analyze the scaffold's response. Material properties, such as Young's modulus of PEGDA, PEGDA-nHAp, and GelMA hydrogel, were obtained through compression testing and are detailed in **Table S1**. During simulation, boundary conditions and constraints matched those used in physical compression tests: the bottom surface of the scaffold was fixed, while a downward displacement of 0.58 mm (equivalent to 10% of the scaffold height) was applied to the top surface. To accurately model interactions, Binding Tie constraints were applied between the hyperboloid lattice structure and the reticulation lattice structure, and Embedded constraints were used between the lattice structure and the hydrogel. The hyperboloid osteochondral scaffold was meshed using

C3D4 elements, with an average mesh size of 0.3; to ensure stability, the mesh size at the intersections of hyperboloid bars was reduced to 0.05.

6. Differentiation of MSCs in hyperboloid osteochondral scaffold during cyclic dynamic compression

To investigate the impact of energy-absorbing properties of hyperboloid lattice structure and the strain regulation effects on cell behavior, MSCs were evenly distributed within GelMA precursor solution and incorporated into the scaffold, creating cell-laden hyperboloid osteochondral scaffolds. GelMA and I2959 were dissolved in cell culture medium to concentrations of 10% and 0.5% (w/v), respectively, and MSCs were suspended at a density of 1×10^6 cells/mL. Using this method, three different scaffold types with embedded cells were prepared: hyperboloid osteochondral scaffold (with hyperboloid structure in the upper layer and reticulation structure in the lower layer), reticulation osteochondral scaffold (with reticulation structure in both layers, the bio-inks were consistent with the hyperboloid osteochondral scaffold), and GelMA hydrogel scaffold (with no internal 3D-printed structure). The scaffolds were fully submerged in complete medium and subjected to cyclic dynamic compression. A bioreactor applied a 5% strain at 1 Hz for 1 hour daily to the scaffolds to simulate cyclic loading. Live/dead staining was performed after 1, 4, and 7 days of culture using an activity/cytotoxicity kit (Invitrogen, Carlsbad, CA, USA) and observed under confocal fluorescence microscopy. To explore the influence of adaptive strain microenvironment on cell differentiation, which was provided by hyperboloid structure under dynamic compression, immunofluorescence staining was conducted on days 7 and 21 to assess the expression of chondrogenic markers (SOX9, COL II) and osteogenic markers (Runx2, COL I). The gene expression of chondrogenic markers (SOX9, COL II) and osteogenic markers (RunX2, COL I) was analyzed using qPCR after 21 days of culture. Meanwhile, Safranin-O and Alcian blue staining were employed to detect the secretion of proteoglycans and glycosaminoglycans, while Alizarin red staining was used to evaluate the formation of calcium nodules. Static cultivation was used as control.

7. In vivo evaluation of MSCs-laden hyperboloid osteochondral scaffold

Rabbit osteochondral defect model was created to evaluate in vivo performance of MSCs-laden hydrogel-composite scaffolds. Thirty-two adult male New Zealand white rabbits (6 months old, weighing approximately 2.5 kg) were selected for this study. The rabbits were randomly assigned to four groups: GelMA hydrogel scaffold group (GelMA), reticulation osteochondral scaffold group (ROS), hyperboloid osteochondral scaffold group (HOS), and an untreated control group (Blank) (n = 8 per group). Anesthesia was administered via intraperitoneal injection of 2% sodium pentobarbital (1.5 mL/kg). An osteochondral defect (5 mm in diameter and 4 mm in depth) was created on both knees of rabbits using an orthopedic drill. The defects sites were continuously flushed with saline containing 1% antibiotics to facilitate the drilling process and prevent overheating. The scaffolds were then implanted into the defect and the blank control was untreated. The incision was then closed with a degradable suture (4-0 silk suture, Ethicon, USA). Postoperatively, each rabbit received an intramuscular injection of penicillin (160,000 IU) daily for 5 days to prevent infection. All animal experiments adhered strictly to the approved guidelines of the Institutional Animal Care and Use Committee (IACUC) at Huazhong University of Science and Technology.

8. Micro-CT analysis

Micro-CT imaging was performed on femur specimens collected from the defect sites to assess osteochondral repair. The specimens were collected at week 6 and week 12 post-surgery and then fixed in 4% paraformaldehyde for 3 days. After being rinsed with PBS, the samples were mounted in foam brackets for scanning. Micro-CT analysis was conducted using a micro-CT 50 scanner (Scanco Medical, Switzerland) with the following parameters: 80 kV source voltage, Cu + Al filter, and an image resolution of 18 μm per pixel. 3D images were reconstructed using multimodal 3D visualization software (Inveon Research Workplace, Siemens, Germany). The cylindrical region of interest (ROI) was selected on the reconstructed images according to the location of the original defects. Moreover, new bone volume (BV), trabecular thickness (Tb.Th) and trabecular number (Tb.N) were measured and calculated.

9. Quantitative reverse transcription-polymerase chain reaction (qRT-PCR)

The qRT-PCR was performed to analyze the expression of genes related to osteogenesis and chondrogenesis, including bone markers (COL I, OCN) and cartilage markers (aggrecan, COL II). Defect regions were harvested from euthanized animals, immediately frozen in liquid nitrogen, and ground into powder. Total RNA was extracted using the E.Z.N.A. HP Total RNA Kit (Omega, BIO-TEK) according to the manufacturer's instructions. The extracted RNA was then reverse-transcribed to complementary DNA (cDNA), and qRT-PCR reactions were conducted using a Real-time fluorescence quantitative PCR instrument (Bio-Rad, USA). The primer sequences for the target genes and the internal control gene (β -actin) were provided in **Table S2**.

10. Western blot and proteomic analysis of defect regions

The defect regions were pulverized under liquid nitrogen, and total proteins were extracted using RIRA lysis buffer. Western blot was utilized to detect the expression levels of chondrogenic proteins (SOX9, COL II) and osteogenic proteins (COL I, OCN, BMP2, Runx2). For proteomic analysis, additional samples were preserved on dry ice and sent to BGI for proteomic analysis. The peptides in the samples were identified and quantitatively analyzed using tandem mass tag (TMT) mass spectrometry. Bioinformatics tools and databases were employed to analyze the mass spectrometry data, perform functional annotation, and conduct pathway analysis of proteins, aiming to elucidate the biological significance of the proteomic data.

11. Histological and immunohistochemical analysis

Following micro-CT analysis, the specimens were decalcified in 15% (w/v) ethylenediaminetetraacetic acid (EDTA), dehydrated through an ethanol series, embedded in paraffin, and sectioned longitudinally into 5 μ m slices using a paraffin microtome (Leica EG 1160). Sagittal sections were stained with hematoxylin and eosin (HE), Safranin O-fast green (S-F) and Alizarin red staining to evaluate histological morphology. The pathological features of the knee joints were evaluated using the International Cartilage Repair Society (ICRS) scoring system by three independent, blinded observers. For immunofluorescence staining, sections were incubated overnight at 4°C with goat polyclonal anti-COL II (Arigo, ARG20787) and rabbit polyclonal anti-COL I (Abcam, USA), followed by incubation with secondary

antibodies for 1 hour, and nuclei were then stained with DAPI. Fluorescence images were captured using confocal fluorescence microscopy to analyze collagen distribution and tissue regeneration.

12. Statistical analysis

All data were presented as means \pm standard deviation (SD). The data were analyzed using SPSS version 22. Statistical analysis was performed using one-way analysis of variance with t-test, and a value of $p < 0.05$ was considered statistically significant.

II. Supporting Figures and Tables

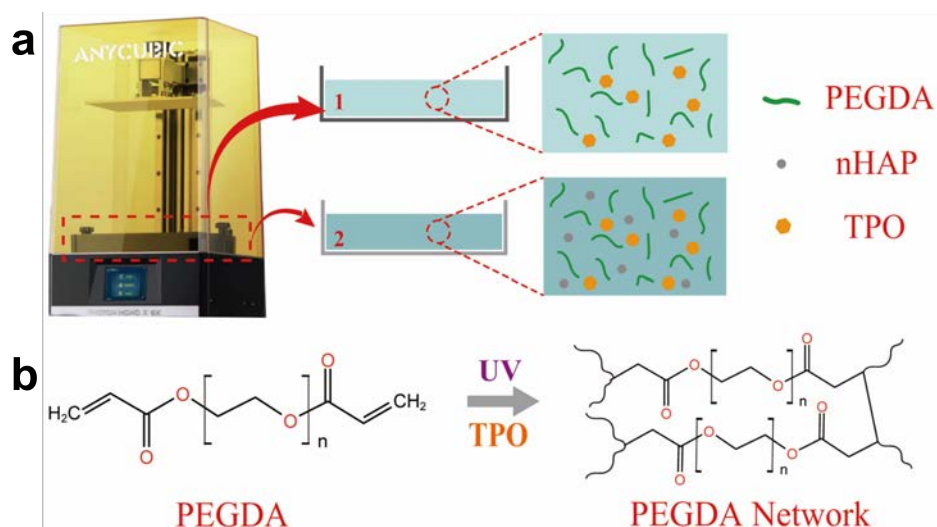


Figure S1. The basic materials of scaffold. (a) The printing ink of hyperboloid lattice structure was composed of PEGDA and TPO, and the printing ink of reticulation lattice structure was composed of PEGDA, nHAP and TPO. **(b)** Photopolymerization mechanism of PEGDA crosslinking network formation.

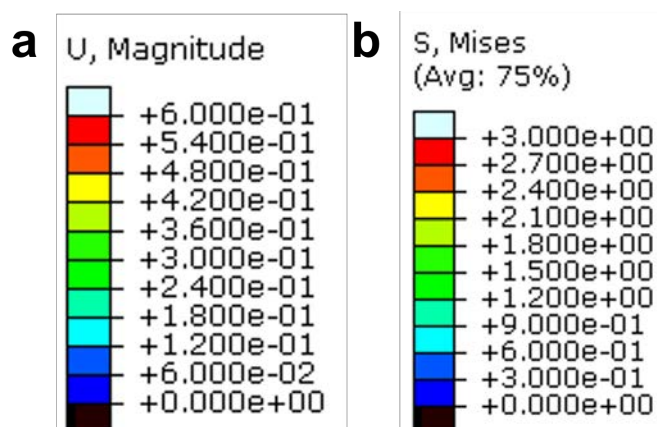


Figure S2. Scale bar for finite element simulation. (a) A scale bar for finite element simulation of the deformation of hyperboloid lattice structure, hyperboloid integrated scaffold and hyperboloid osteochondral scaffold under compressive load. **(b)** A scale bar for finite element simulation of the stress of hyperboloid lattice structure, hyperboloid integrated scaffold and hyperboloid osteochondral scaffold under compressive load.

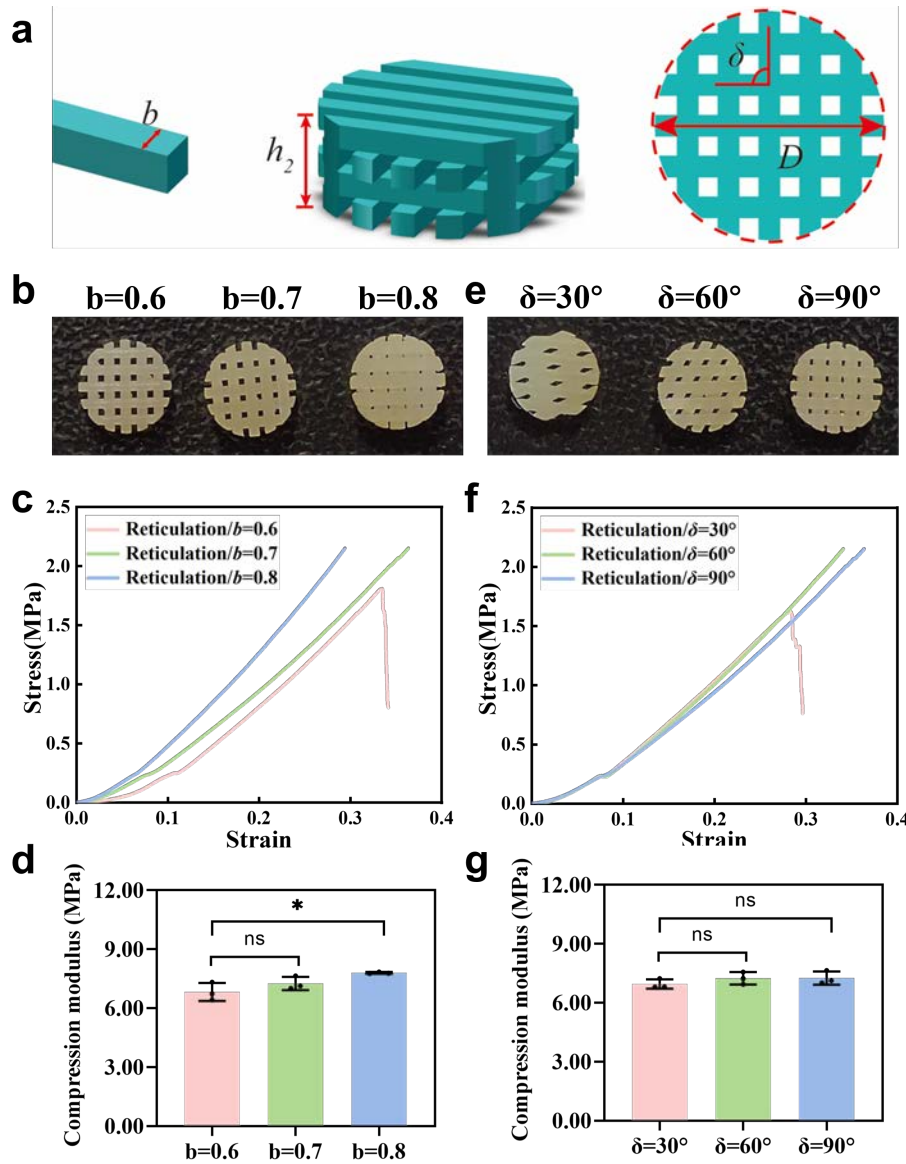


Figure S3. Design and construction of reticulation lattice structures. (a) The design model and parameters of reticulation lattice structures with high mechanical strength. (b) Reticulation lattice structures with different rod diameter ($b = 0.6$ mm, $b = 0.7$ mm and $b = 0.8$ mm) were prepared by 3D printing technology. (c, d) The compression modulus of reticulation lattice structures with different rod diameter were 6.834 ± 0.450 MPa ($b = 0.6$), 7.269 ± 0.329 MPa ($b = 0.7$) and 7.804 ± 0.038 MPa ($b = 0.8$), respectively. (e) Reticulation lattice structures with different rod angle ($\delta = 30^\circ$, $\delta = 60^\circ$ and $\delta = 90^\circ$) were prepared by 3D printing technology. (f, g) The compression modulus of reticulation lattice structures with different rod angle were 6.965 ± 0.234 MPa ($\delta = 30^\circ$), 7.256 ± 0.309 MPa ($\delta = 60^\circ$) and 7.269 ± 0.329 MPa ($\delta = 90^\circ$), respectively.

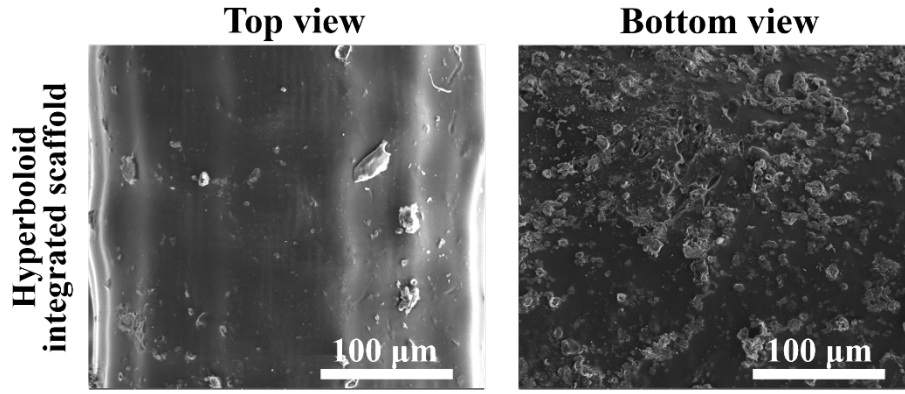


Figure S4. SEM images of the top and bottom views of the hyperboloid integrated scaffold.

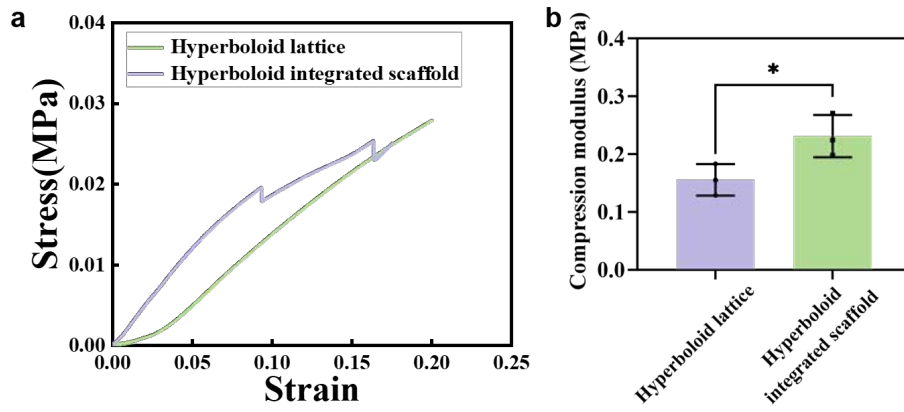


Figure S5. Mechanical evaluation of hyperboloid integrated scaffold. (a) The stress-strain curve of the hyperboloid lattice and hyperboloid integrated scaffold. (b) The compressive modulus of the hyperboloid structure was 0.156 ± 0.027 MPa, while that of the hyperboloid integrated scaffold was 0.231 ± 0.066 MPa.

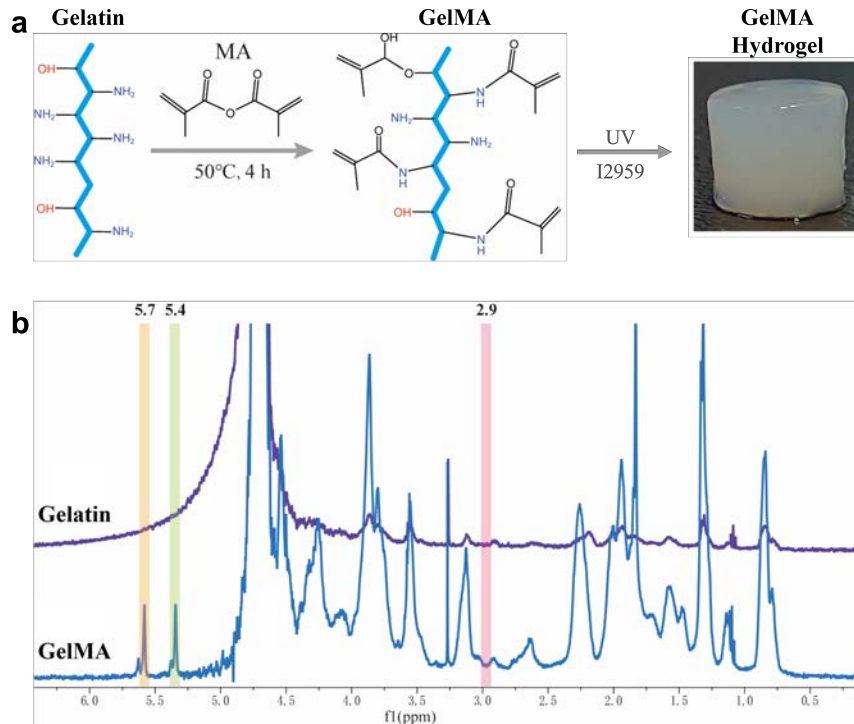


Figure S6. Synthesis and characterization of GelMA. (a) Schematic diagram of GelMA synthesis from gelatin. (b) Nuclear magnetohydrogen spectra of Gelatin and GelMA showed that MA was successfully grafted onto gelatin.

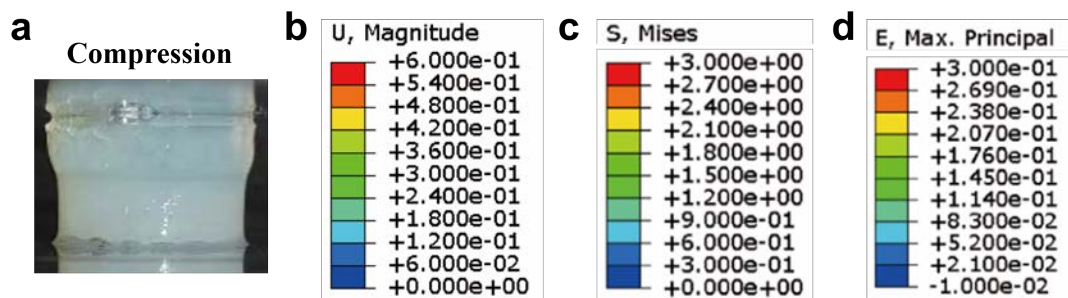


Figure S7. Scale bar for finite element simulation. (a) At 10% strain, the hydrogel inside the hyperboloid osteochondral scaffold produced significant lateral expansion. (b-d) Scale bar for finite element simulation of displacement, stress and strain.

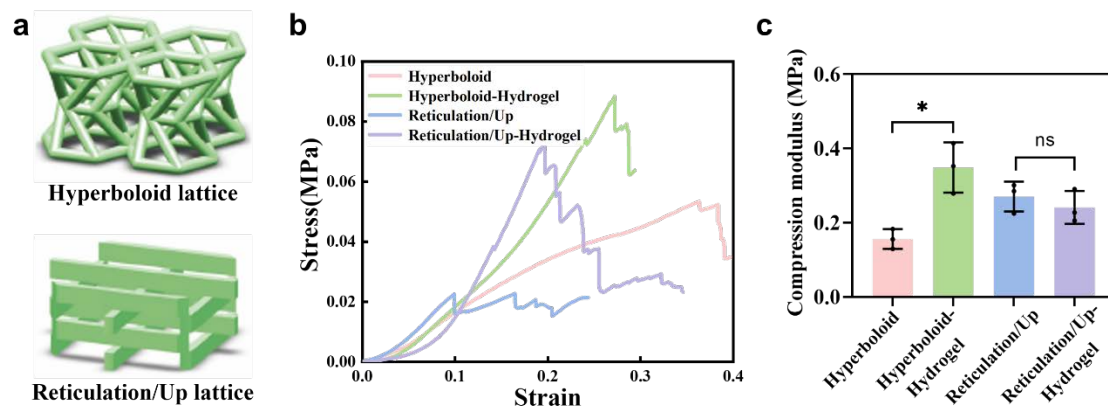


Figure S8. Mechanical properties tests of hydrogel-composite scaffolds. (a) The Reticulation/Up lattice structure was printed using the same materials (PEGDA and TPO) as the hyperboloid lattice structure. (b) Stress-strain curves of Hyperboloid, Hyperboloid-Hydrogel, Reticulation/Up and Reticulation/Up-Hydrogel scaffolds. (c) The compression modulus of Hyperboloid, Hyperboloid-Hydrogel, Reticulation/Up and Reticulation/Up-Hydrogel scaffolds was 0.156 ± 0.027 MPa, 0.348 ± 0.067 MPa, 0.270 ± 0.040 MPa and 0.240 ± 0.044 MPa, respectively.

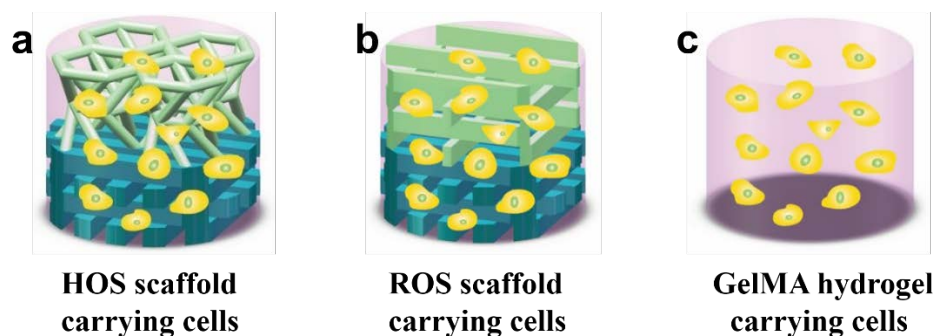


Figure S9. The hydrogel-composite scaffolds carrying MSCs. (a) The hyperboloid osteochondral scaffold (HOS scaffold) carrying MSCs. (b) The reticulation osteochondral scaffold (ROS scaffold) carrying MSCs. (c) The GelMA hydrogel scaffold carrying MSCs.



Figure S10. The bioreactor with cyclic compression function. In the blue frame is the external drive motor of the compression unit. In the red box is compression device applying pressure to the scaffold in the cell culture plate.

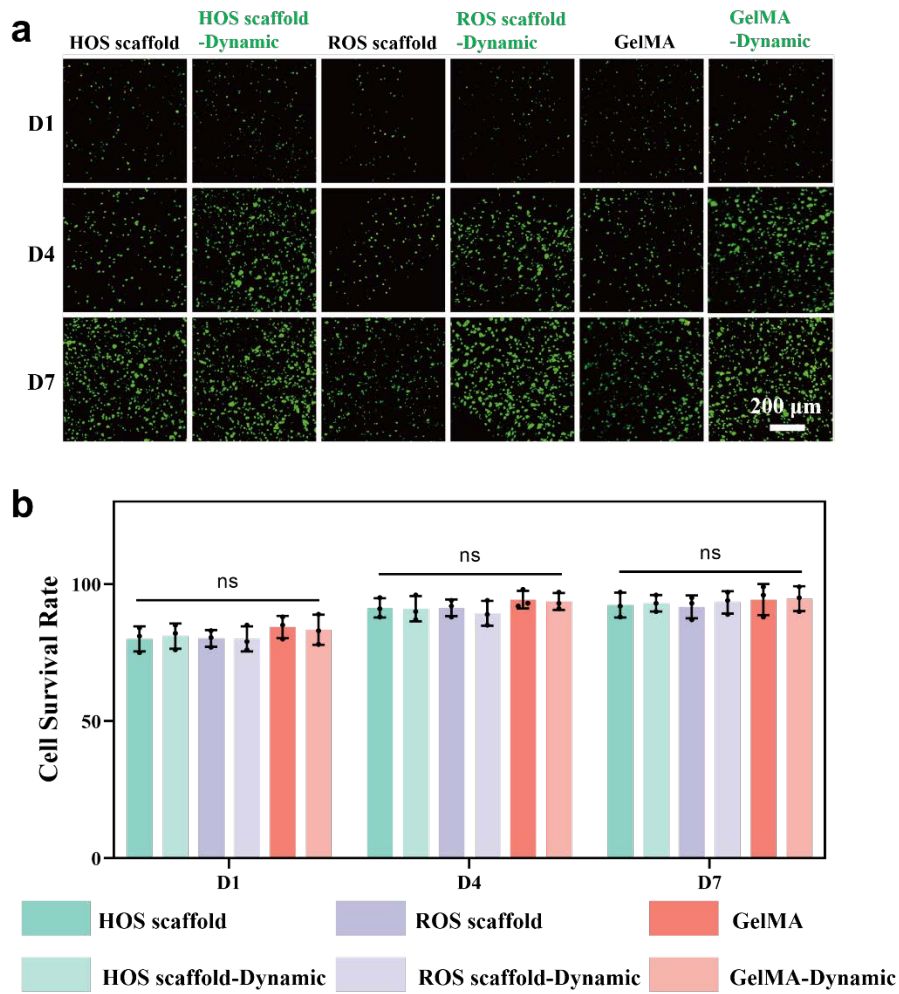


Figure S11. Bioactivity of cells in scaffolds under dynamic and static mechanical conditions. (a) The results of Live-Dead staining after 1, 4 and 7 days of continuous culture showed that MSCs in scaffolds could proliferate normally under both dynamic and static mechanical conditions. **(b)** The survival rate of cells in scaffolds increased gradually from day 1 to day 7, indicating that scaffolds had good biocompatibility.

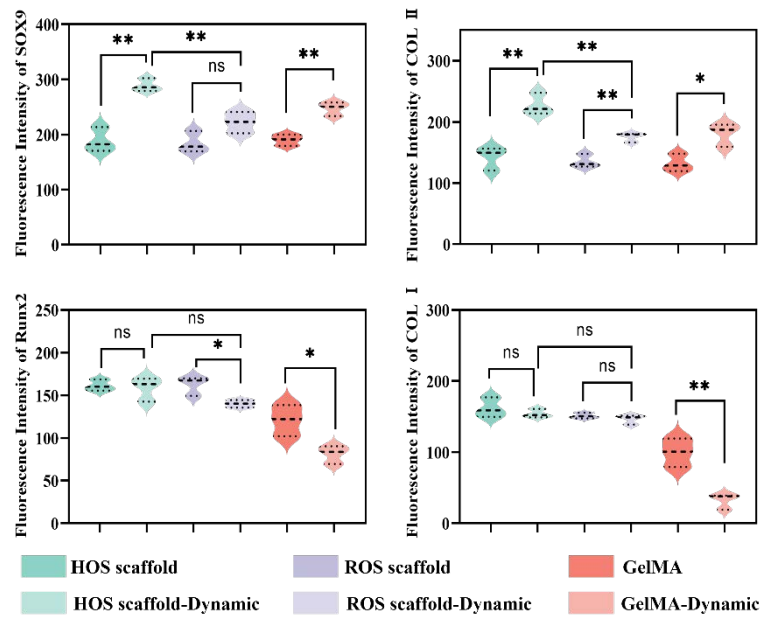


Figure S12. Semi-quantitative immunofluorescence analysis of chondrocyte-specific proteins (SOX9, COL II) and osteoblast-specific proteins (Runx2, COL I) exhibited the consistent results with IF under dynamic and static conditions.

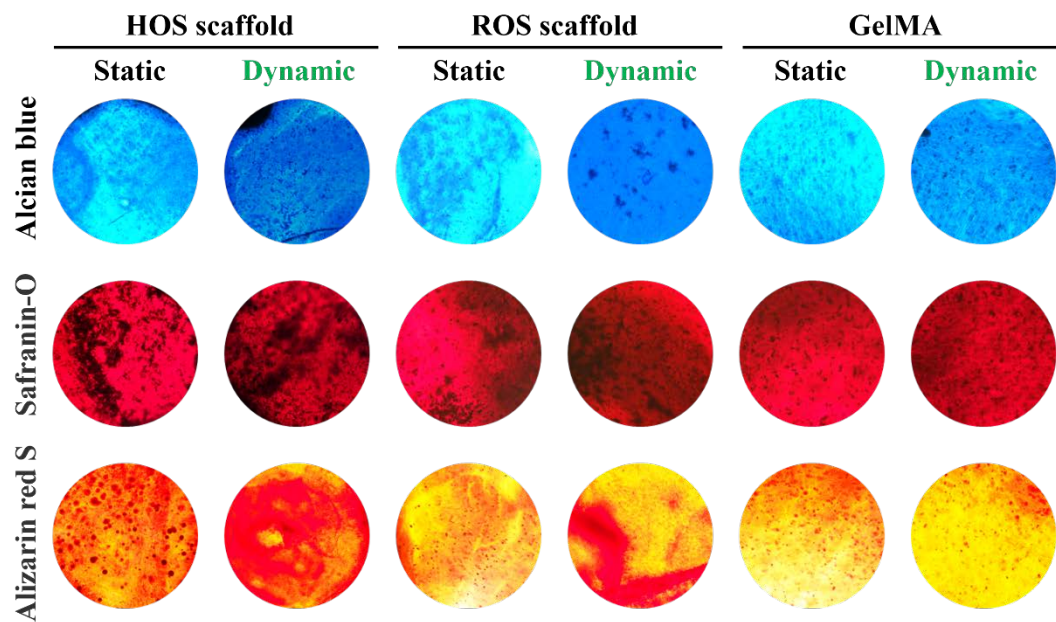


Figure S13. The staining results of alcian blue, safranin-O and alizarin red confirmed that cyclic dynamic compression promoted osteogenic differentiation and chondrogenic differentiation of MSCs in the hyperboloid osteochondral scaffolds.

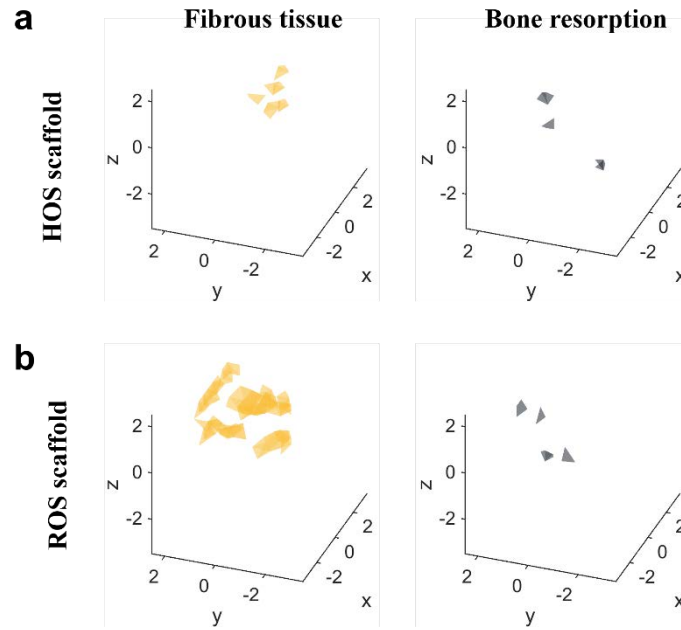


Figure S14. Finite element simulation of cell differentiation under cyclic dynamic compression. (a, b) Compared with hyperboloid osteochondral scaffold, fibrous connective tissue differentiation and bone absorption occurred more frequently in reticulation osteochondral scaffold.

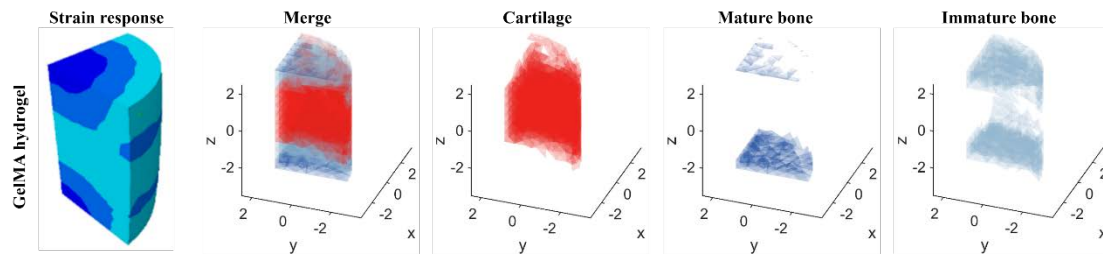


Figure S15. Finite element simulation of cell differentiation under cyclic dynamic compression in GelMA hydrogel scaffold. Most cells in the middle part of the GelMA hydrogel scaffold differentiated into cartilage, while the upper and lower ends differentiated into immature bone and mature bone.

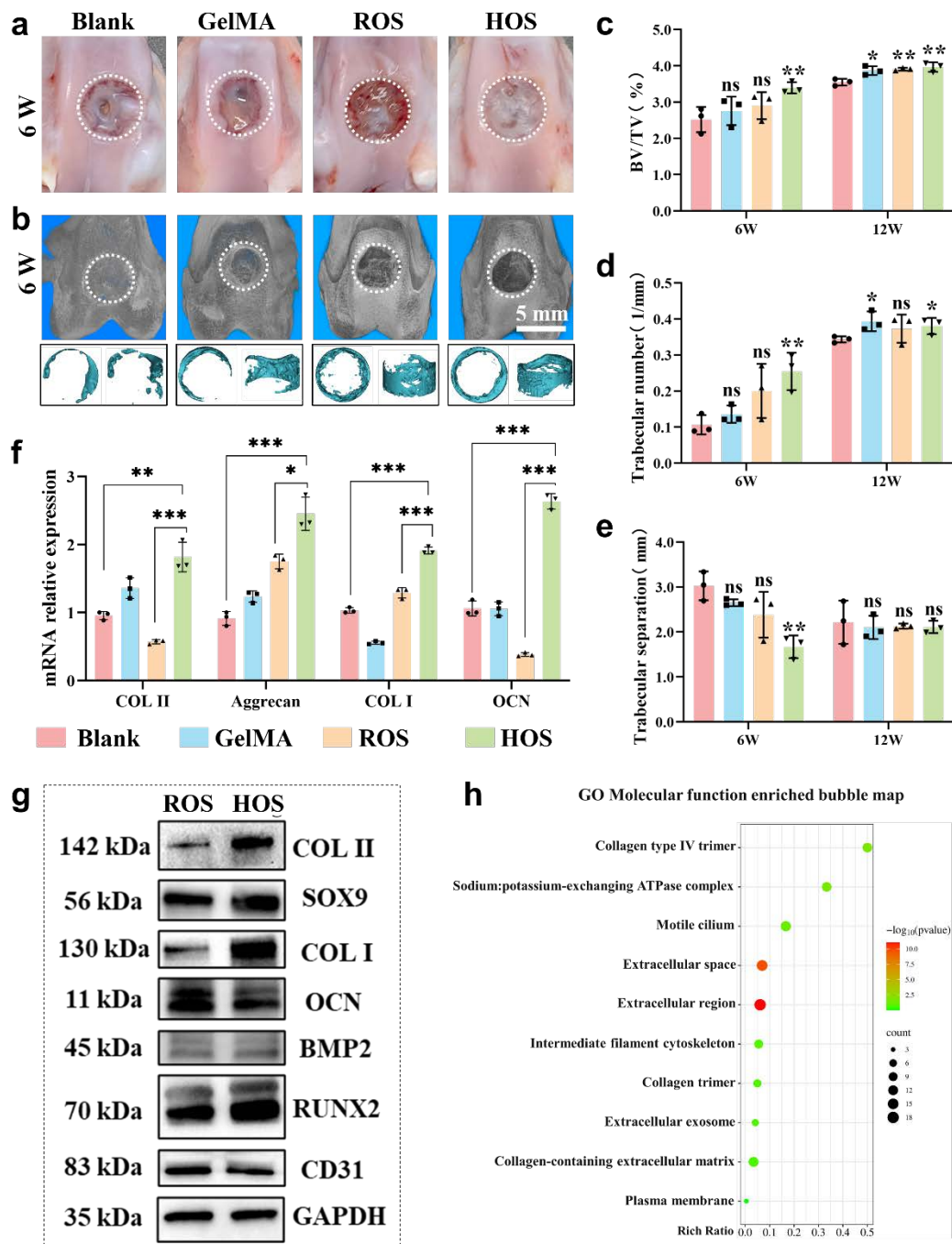


Figure S16. Hyperboloid osteochondral scaffolds carrying MSCs promoted cartilage and subchondral bone regeneration in rabbits. (a) Macroscopic appearance showed that the cartilage repair in HOS group was superior to that in other groups after 6 weeks post-surgery. (b) Micro-CT evaluation of the Blank, GelMA, ROS and HOS groups after 6 weeks post-surgery. (c-e) Quantitative micro-CT data further verified that the total bone volume (BV/TV) and the number of bone trabecula (Tb. N) were the highest in the HOS group. (f) qRT-PCR results after 6 weeks post-surgery showed that the expression levels of cartilage-associated genes (COL II and aggrecan) and osteogenesis-associated genes (COL I and OCN) were the highest in the HOS group. (g) The protein expression of the ROS and HOS groups was detected by Western Blot after 12 weeks post-surgery. (h) GO enrichment analysis verified the regulation pathway of HOS scaffold was associated with collagen type IV trimer, extracellular space and region.

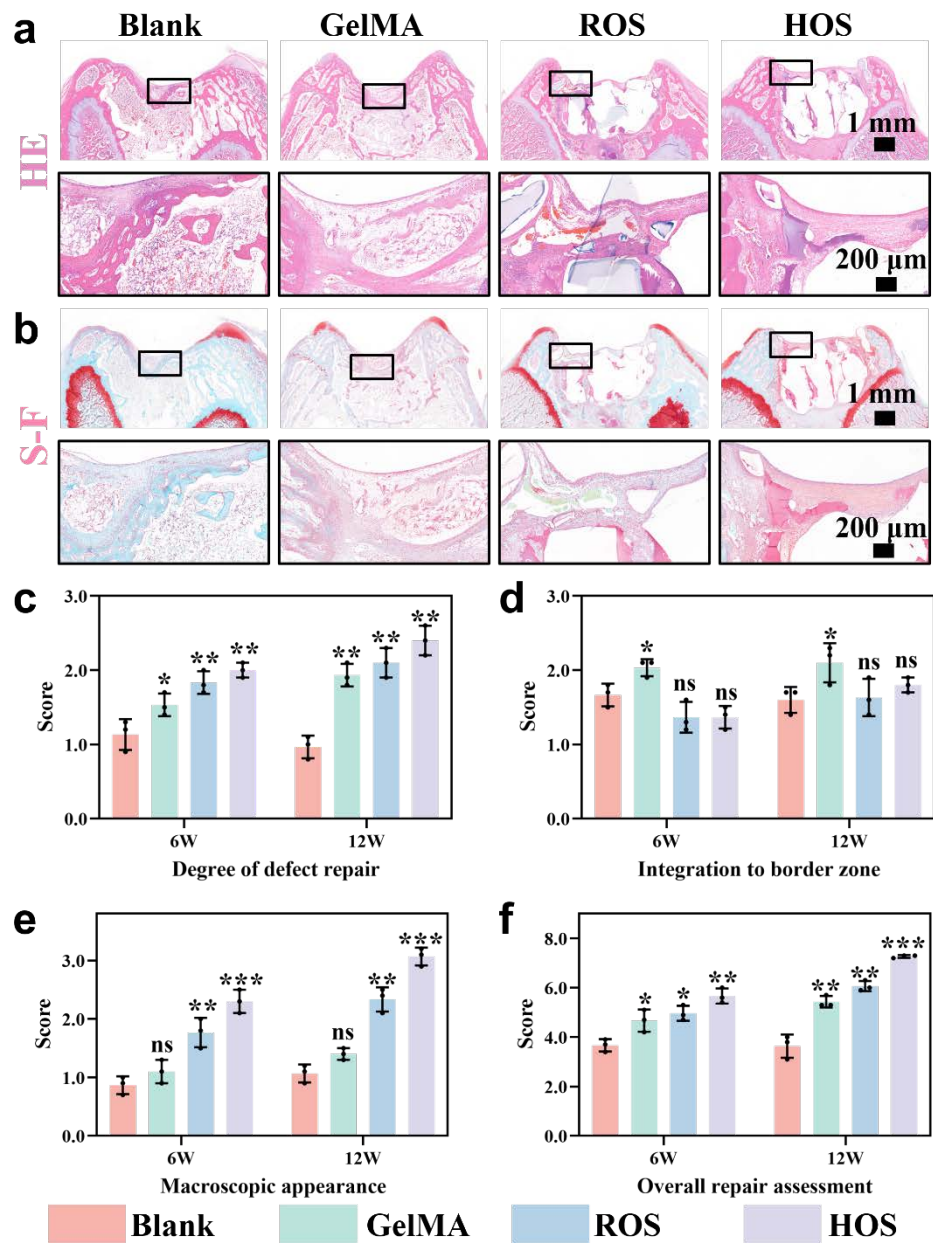


Figure S17. Histological staining and immunofluorescence staining of cartilage regeneration. (a, b) H&E and S-F staining after 6 weeks post-surgery revealed that the defect area in the Blank and GelMA groups was full of new tissue, but not bone and cartilage, compared to the ROS and HOS groups. (c-f) ICRS histological scores (Degree of defect repair, Integration to border zone, Macroscopic appearance, Overall repair assessment) of the Blank, GelMA, ROS and HOS groups after 6 weeks and 12 weeks post-surgery.

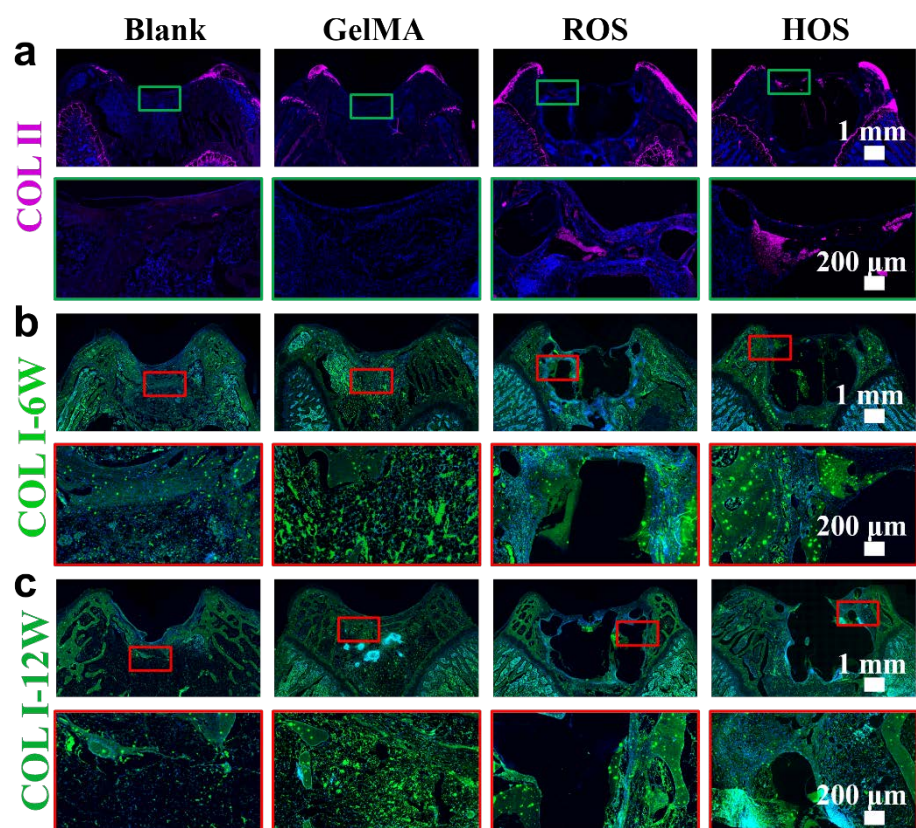


Figure S18. Immunofluorescence staining of bone regeneration. (a) Immunofluorescence staining of COL II of the Blank, GelMA, ROS and HOS groups after 6 weeks post-surgery. (b) Immunofluorescence staining of COL I after 6 weeks post-surgery. (c) Immunofluorescence staining of COL I after 12 weeks post-surgery.

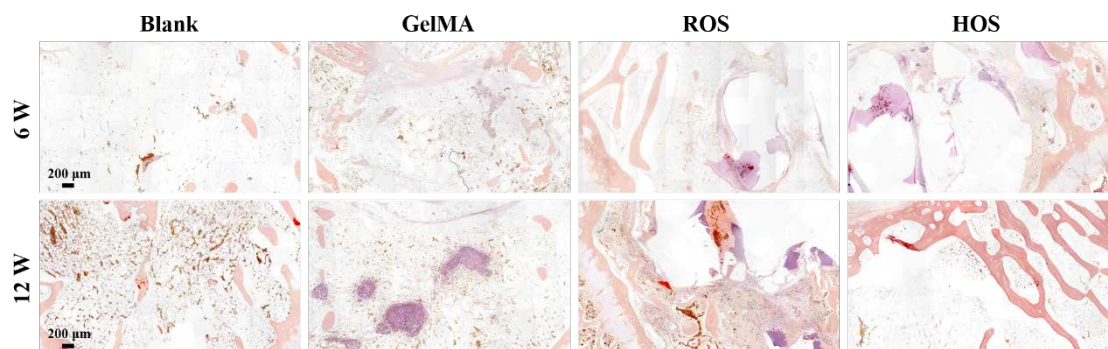


Figure S19. The HOS scaffold significantly improved subchondral bone regeneration, as evidenced by alizarin red staining at 6 weeks and 12 weeks post-implantation.

Table S1. The attribute parameters of each material used in the simulation process

Attribute parameters	PEGDA	PEGDA-nHAP	GelMA Hydrogel
Young's modulus (MPa)	8	8.7	0.027
Poisson's ratio	0.3	0.3	0.45

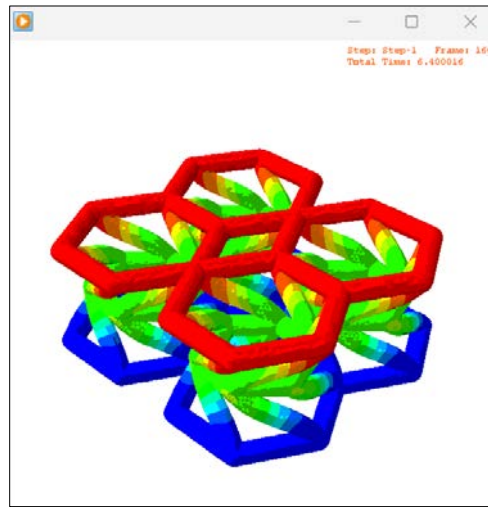
Table S2. Primer sequences of targeted genes for qRT-PCR

Genes	Primer sequence (5'-3')	Product size (bp)
β -actin	FWD: CGAGATCGTGCGGGACAT	184
	REV: CAGGAAGGAGGGCTGGAAC	
Aggrecan	FWD: CATCTGGAGTTCTTTTGGGAG	122
	REV: CAGGTCAGGGATTCTGTGTGTC	
Collagen I	FWD: TGAAGACACCAAGGACTGCC	150
	REV: TTCTTGCTGATGTACCAGTTCTTCTGGG	
Collagen II	FWD: TGAAGACACCAAGGACTGCC	81
	REV: GCAGTGGCGAGGTCAGTAG	
OCN	FWD: CAAAGCCCAGCGGTGCAGAGTCT	110
	REV: AGCTCCCTGCCCCGTCGATCAGTT	

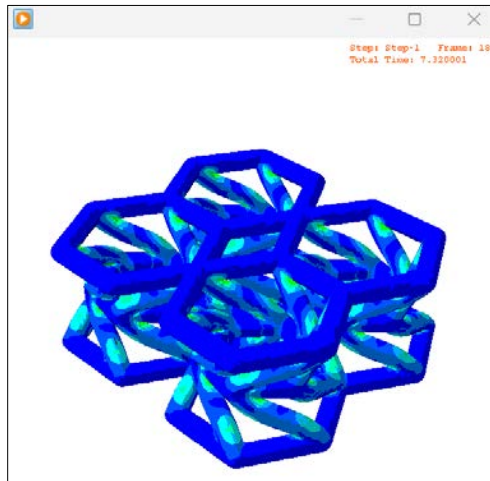
Table S3. S and its corresponding tissue differentiation results

S	Tissue differentiation
$0 < S < 0.01$	Bone resorption
$0.01 < S < 0.53$	Mature bone
$0.53 < S < 1$	Immature bone
$1 < S < 3$	Cartilage
$S > 3$	Fibrous tissue

III. Supporting Videos

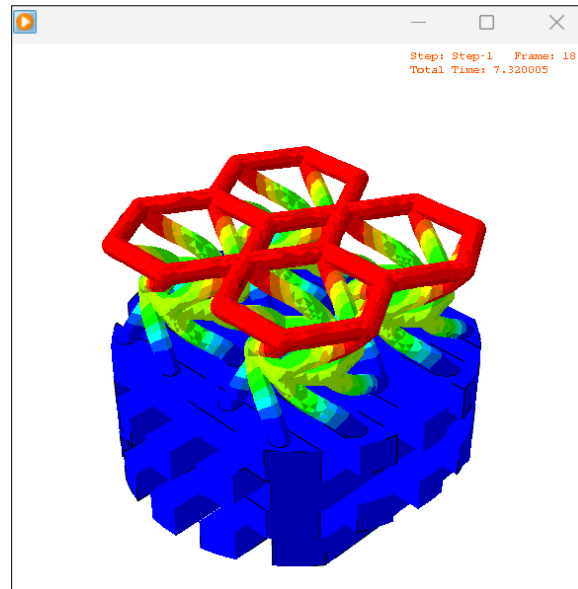


Video S1

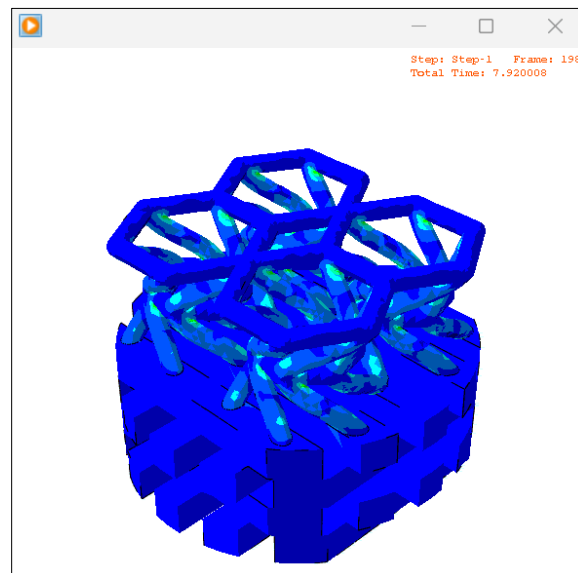


Video S2

Video S1, S2: Finite element simulations showed the displacement (**Video S1**) and stress distribution (**Video S2**) within the hyperboloid lattice under compressive load.

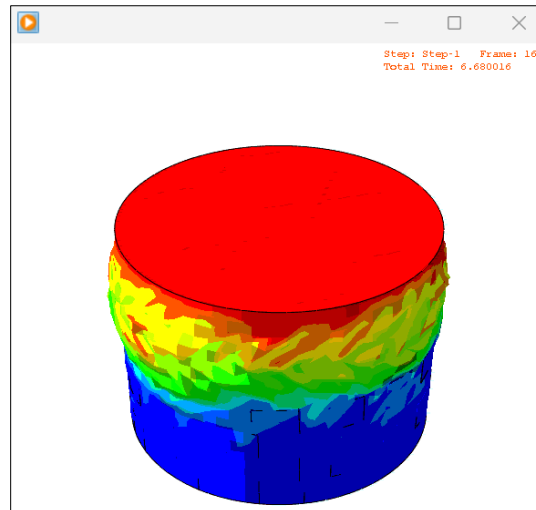


Video S3

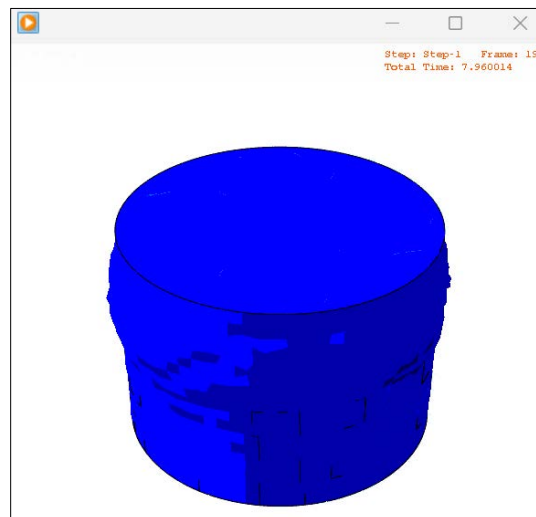


Video S4

Video S3, S4: Finite element analysis demonstrated that displacement and stress under compressive load were primarily concentrated in the upper hyperboloid structure, supporting its role in energy absorption and shock buffering.

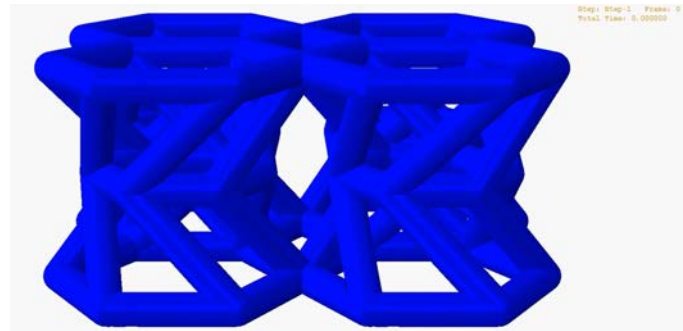


Video S5

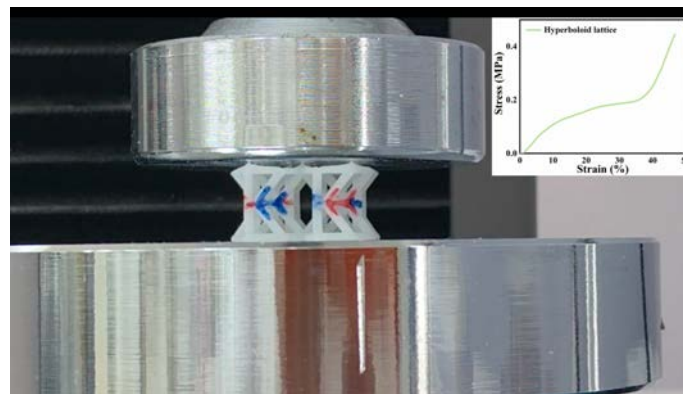


Video S6

Video S5, S6: Finite element analysis exhibited that the hydrogel in the upper hyperboloid structure exhibited noticeable lateral expansion during compression (**Video S5**), while the stress distribution remained concentrated in the upper layer, emphasizing the buffering capacity of the hyperboloid structure (**Video S6**).



Video S7



Video S8

Video S7, S8: The simulation (**Video S7**) and experimental (**Video S8**) videos employed close-up shots to highlight the rotation and deformation behaviors during the compression process.